21121

NATIONAL LIBRARY
OTTAWA

BIBLIOTHÈQUE NATIONALE
OTTAWA

NAME OF AUTHOR....MARIELLA...TATRALLYAY.....

TITLE OF THESIS. THE..PERTURBATION..OF..AN..ALTERNATING
.ELECTROMAGNETIC..FIELD..BY..TWO-DIMENSIONAL
.CONDUCTIVITY..MODELS..IN..A..CYLINDRICAL..CO-ORDINATE
SYSTEM.

UNIVERSITY...THE..UNIVERSITY..OF..ALBERTA.....

DEGREE FOR WHICH THESIS WAS PRESENTED..M..Sc.....

YEAR THIS DEGREE GRANTED...1974.....

Permission is hereby granted to THE NATIONAL LIBRARY OF CANADA to microfilm this thesis and to lend or sell copies of the film.

The author reserves other publication rights, and neither the thesis nor extensive extracts from it may be printed or otherwise reproduced without the author's written permission.

(Signed) Mariella Tatrallyay...

PERMANENT ADDRESS:

Geod. and Geophys...
Research Inst.....
...Sopron, Hungary.

DATED. Dec. 12, ...1973

NL-91 (10-68)

THE UNIVERSITY OF ALBERTA

THE PERTURBATION OF AN ALTERNATING ELECTROMAGNETIC FIELD BY TWO-DIMENSIONAL CONDUCTIVITY MODELS IN A CYLINDRICAL CO-ORDINATE SYSTEM

by

© MARIELLA TATRALLYAY

A THESIS

SUBMITTED TO THE FACULTY OF GRADUATE STUDIES AND RESEARCH

IN PARTIAL FULFILLMENT OF THE REQUIREMENTS FOR THE DEGREE

OF MASTER OF SCIENCE

DEPARTMENT OF PHYSICS

EDMONTON, ALBERTA

SPRING, 1974

THE UNIVERSITY OF ALBERTA

FACULTY OF GRADUATE STUDIES AND RESEARCH

The undersigned certify that they have read, and recommend to the Faculty of Graduate Studies and Research, for acceptance, a thesis entitled THE PERTURBATION OF AN ALTERNATING ELECTROMAGNETIC FIELD BY TWO-DIMENSIONAL CONDUCTIVITY MODELS IN A CYLINDRICAL CO-ORDINATE SYSTEM, submitted by Mariella Tatrallyay in partial fulfillment of the requirements for the degree of Master of Science.

.....
Supervisor

.....

.....

Douglas M. Sheppard

.....

Date November 30, 1973

ABSTRACT

The perturbations of alternating geomagnetic fields of global dimensions by two-dimensional local structures is studied in a cylindrical co-ordinate system. A general numerical finite difference technique is applied to solve Maxwell's equations at each point of a polar mesh with variable grid spacings.

The proper size and spacing of the mesh used for different conductivity configurations is discussed with respect to the Gauss-Seidel iterative method which is used to solve the finite difference equations.

Two symmetric models, one a ridge-like structure and the other a dyke, are studied for different oscillation periods of the source. A series of sloping contacts with different slopes is investigated as well. In the H-polarization case the magnetic field and in the E-polarization the electric field is given over the non-uniform region at different epochs of the oscillation period. Also, the electric and magnetic field components as well as the apparent resistivity and the ratio of the vertical and horizontal magnetic components are calculated along the surface. These profiles are discussed in detail.

ACKNOWLEDGEMENTS

I wish to express my sincere thanks to my supervisor, Dr. F. W. Jones for his guidance and assistance in this study.

I also wish to express my appreciation to Dr. D. I. Gough and Dr. J. A. Jacobs for their encouragement and support.

I am indebted to Mrs. Carol Fryer for her help in computer programming and to Mrs. Lee Cech for typing this thesis.

Finally, I acknowledge the financial support of the Department of Physics, University of Alberta in the form of a Teaching Assistantship.

TABLE OF CONTENTS

		Page
CHAPTER 1	INTRODUCTION	1
1.1	Historical Background	1
1.2	General Outline of the Study	2
CHAPTER 2	MATHEMATICAL FORMULATION OF THE ELECTROMAGNETIC PROBLEM IN A CYLINDRICAL CO-ORDINATE SYSTEM	5
2.1	Basic Equations	5
2.2	The Numerical Method	8
2.3	Internal Boundary Conditions	10
	2.3.1 General	10
	2.3.2 H-polarization	11
	2.3.3 E-polarization	14
2.4	Boundary Conditions at the Surface	15
	2.4.1 H-polarization	15
	2.4.2 E-polarization	16
CHAPTER 3	GENERAL DISCUSSION OF THE COMPUTATIONS	18
3.1	Initial Values for the Iteration	18
3.2	The Grid	20
3.3	Calculation of the Surface Values	24
3.4	The Iteration Procedure	30

		Page
CHAPTER 4	RESULTS FROM THREE TWO-DIMENSIONAL MODELS	37
4.1	General Description of the Results	37
4.2	The Ridge Model	43
4.2.1	General	43
4.2.2	H-polarization	45
4.2.3	E-polarization	49
4.3	The Dyke Model	55
4.3.1	General	55
4.3.2	H-polarization	57
4.3.3	E-polarization	61
4.4	The Sloping Contact Model	66
4.4.1	General	66
4.4.2	H-polarization	69
4.4.3	E-polarization	74
CHAPTER 5	CONCLUSIONS	85
REFERENCES		87

LIST OF TABLES

Table		Page
1	Grid Spacings for the Ridge Model	44
2	Grid Spacings for the Dyke Model	56
3	The Radial Grid Spacings for the Sloping Contacts	67
4	The Angular Grid Spacings for the Sloping Contacts	68

LIST OF FIGURES

Figure		Page
1	The cylindrical co-ordinate system.	6
2	An arbitrary part of the mesh surrounding gridpoint '0' .	6
3	The location of gridpoints near the surface.	6
4	The meshes used.	21
5	The surface values of H_r and ρ_z for the sloping contact models with $\tan \alpha_2 = 0.2$ and $\tan \alpha_5 = \infty$ in the E-polarization case.	29
6	The surface values of E_r for the sloping contact models with $\tan \alpha_1 = 0.1$ and $\tan \alpha_5 = \infty$ in the H-polarization case.	34
7	The surface values of H_r and H_ϕ for the sloping contact models with $\tan \alpha_2 = 0.2$ and $\tan \alpha_5 = \infty$ in the E-polarization case.	35
8	The ridge model.	38
9	The dyke model.	38
10	The sloping contact models.	39
11	Ridge model, H-polarization. Amplitude contours of H_z.	46
12	Ridge model, E-polarization. Amplitude contours of E_z.	46
13	Ridge model, H-polarization. Contours of equal H_z at equal intervals of one-sixteenth of the period.	47
14	Ridge model, H-polarization. Amplitude and phase profiles of E_r and ρ_r.	48
15	Ridge model, E-polarization. Contours of equal E_z at equal intervals of one-sixteenth of the period for the first four epochs.	50

Figure		Page
16	Ridge model, E-polarization. Contours of equal E_z at equal intervals of one-sixteenth of the period for the second four epochs.	51
17	Ridge model, E-polarization. Amplitude and phase profiles of E_z and H_ϕ .	53
18	Ridge model, E-polarization. Amplitude and phase profiles of H_r, H_ϕ/H_r and ρ_z .	54
19	Dyke model, H-polarization. Amplitude contours of H_z .	58
20	Dyke model, E-polarization. Amplitude contours of E_z .	58
21	Dyke model, H-polarization. Contours of equal H_z at equal intervals of one-sixteenth of the period.	59
22	Dyke model, H-polarization. Amplitude and phase profiles of E_r and ρ_r .	60
23	Dyke model, E-polarization. Contours of equal E_z at equal intervals of one-eighth of the period.	62
24	Dyke model, E-polarization. Amplitude and phase profiles of E_z and ρ_z .	64
25	Dyke model, E-polarization. Amplitude and phase profiles of H_ϕ, H_r and H_ϕ/H_r .	65
26	Sloping contact models, H-polarization. Amplitude contours of H_z .	70
27	The sloping contact model with $\tan \alpha_4 = 1.0$, H-polarization. Contours of equal H_z at equal intervals of one-sixteenth of the period.	72
28	Sloping contact models, H-polarization. Amplitude and phase profiles of E_r and ρ_r .	73

Figure		Page
29	Sloping contact models, E-polarization. Amplitude contours of E_z.	76
30	The sloping contact model with $\tan \alpha_4 = 1.0$, E-polarization. Contours of equal E_z at equal intervals of one-eighth of the period.	77
31	Sloping contact models, E-polarization. Amplitude and phase profiles of ρ_z and H_ϕ/H_r using set A in Table 3 for the radial grid spacings of the mesh.	78
32	Sloping contact models, E-polarization. Amplitude and phase profiles of E_z, H_r and H_ϕ using set A in the grid.	79
33	Sloping contact models, E-polarization. Amplitude and phase profiles of ρ_z and H_ϕ/H_r using set B in Table 3 for the radial grid spacings of the mesh.	80
34	Sloping contact models, E-polarization. Amplitude and phase profiles of E_z, H_r and H_ϕ using set B in the grid.	81

CHAPTER 1 INTRODUCTION

1.1 Historical Background

Many studies have been made to determine the perturbations of alternating electromagnetic fields by different geological configurations. Some authors have approached the problem analytically (d'Erceville and Kunetz, 1962; Weaver, 1963; Blake, 1970; Weaver and Thomson, 1972; Geyer, 1972) while others have made analogue model measurements (Neves, 1957; Dosso, 1966). Several studies have applied numerical methods to obtain solutions for Maxwell's equations. Some of the most often used of these latter methods are the finite difference technique (Neves, 1957; Patrick and Bostick, 1969; Jones and Price, 1970, 1971a, 1971b; Jones and Pascoe, 1971; Pascoe and Jones, 1972), the transmission line analogy (Madden and Thompson, 1965; Wright, 1969) and the finite element method (Coggon, 1971; Reddy and Rankin, 1973).

Since many geological structures are of two-dimensional nature, such an approach to the geomagnetic induction problem has often been taken, and in most of these works the Cartesian co-ordinate system has been used. In some cases, especially when sloping contact models are studied, it seems more reasonable to use a cylindrical

co-ordinate system. Geyer (1972) considered analytically a sloping contact in cylindrical co-ordinates, but found it necessary to assume that the tangential component of the magnetic field in the E-polarization case is constant all along the surface. However, as discussed by Jones and Price (1970) this approximation is not adequate to describe the true nature of the fields.

The finite element method using triangular meshes is one approximation to the sloping contact model. Reddy and Rankin (1973) gave some general conclusions concerning the electric and magnetic field values along the surface for a contact which is initially sloping but becomes horizontal. However, in their paper very little detail of the mesh dimensions or number of gridpoints is given. It is therefore appropriate to investigate some of these conclusions further, and in particular with reference to a purely sloping contact.

It is reasonable to approach the problem by applying the finite difference method in a cylindrical co-ordinate system. This is suitable for a purely sloping contact and can also be used for other models of interest.

1.2 General Outline of the Study

The problem is to determine the electric and magnetic fields associated with currents induced in the Earth by given geomagnetic sources. When limited areas are

concerned, the Earth can be treated as a semi-infinite composite conductor which may have horizontal layers and lateral inhomogeneities and has a plane surface. This local problem may be considered as a perturbation problem (Price, 1964). The induced field is determined by the local redistribution of a current system of large dimensions. This global inducing field is uniform and has the same intensity and form all over the region considered. In the present study the source field shows sinusoidal time variation.

The work of this thesis is concerned with the numerical solution of the perturbation problem in cylindrical co-ordinates where the conductivity configuration does not change in the z direction. This implies that the problem is of two-dimensional nature and a polar mesh is used. Maxwell's equations are solved at each gridpoint applying the finite difference technique. The method is general so that the sloping contact as well as other conductivity configurations may be studied. In particular a buried ridge-like upwelling (Figure 8) and a dyke-like structure (Figure 9) as well as five different sloping contacts (Figure 10) are examined here. The electric and magnetic field distributions within and outside the conducting region are studied as well as the nature of the current flow associated with the inhomogeneities for two polarization cases.

The surface profiles of the electric and magnetic fields are of particular interest since the field components induced by ionospheric and magnetospheric sources may be measured above natural geological configurations by the magnetotelluric and other methods. Large geological structures which exist naturally can be recognized by comparing observed data with computed electromagnetic perturbation models.

CHAPTER 2 MATHEMATICAL FORMULATION OF THE ELECTROMAGNETIC PROBLEM IN A CYLINDRICAL CO-ORDINATE SYSTEM

2.1 Basic Equations

The co-ordinate system is shown in Figure 1. Maxwell's equations are solved in this system where the conductivity configuration and all field values are constant in the z direction. Since displacement currents may be ignored for the frequencies of the geomagnetic variations considered (Lahiri and Price, 1939), Maxwell's equations become

$$\text{curl } \underline{E} = - i\mu\omega\underline{H} \tag{2.1}$$

$$\text{curl } \underline{H} = k\sigma\underline{E} \tag{2.2}$$

where it is assumed that the time factor for all field quantities is $\exp(i\omega t)$. In electromagnetic units $\mu = 1$ and $k = 4\pi$, while in MKS units $\mu = 4\pi \times 10^{-7}$ and $k = 1$.

As $\underline{E}$ and $\underline{H}$ are independent of z, the six equations for (2.1) and (2.2) are

$$\frac{1}{r}\frac{\partial E_z}{\partial \phi} = - i\omega\mu H_r \tag{2.1a}$$

$$\frac{\partial E_z}{\partial r} = i\omega\mu H_\phi \tag{2.1b}$$

$$\frac{1}{r}\frac{\partial (rE_\phi)}{\partial r} - \frac{1}{r}\frac{\partial E_r}{\partial \phi} = - i\omega\mu H_z \tag{2.1c}$$

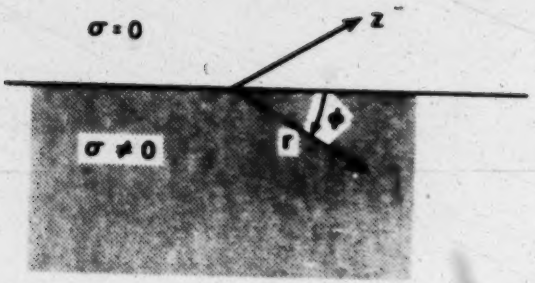

Figure 1 The cylindrical co-ordinate system.

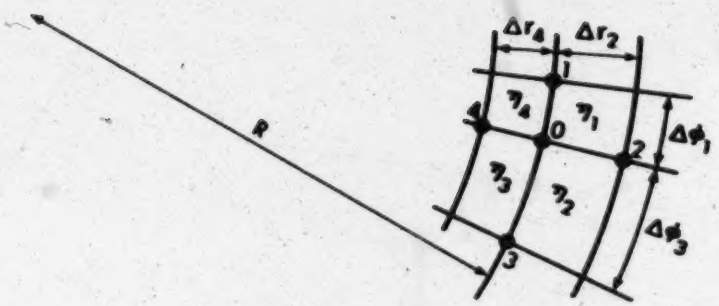

Figure 2 An arbitrary part of the mesh surrounding gridpoint '0'.

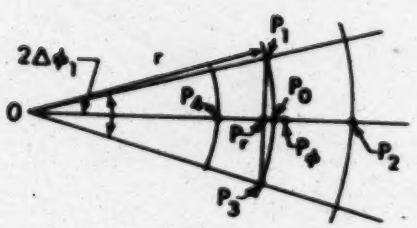

Figure 3 The location of gridpoints near the surface.

$$\frac{1}{r}\frac{\partial H_z}{\partial \phi} = k\sigma E_r \tag{2.2a}$$

$$-\frac{\partial H_z}{\partial r} = k\sigma E_\phi \tag{2.2b}$$

$$\frac{1}{r}\frac{\partial (rH_\phi)}{\partial r} - \frac{1}{r}\frac{\partial H_r}{\partial \phi} = k\sigma E_z \tag{2.2c}$$

Equations (2.1c), (2.2a) and (2.2b) involve only H_z, E_r and E_ϕ and represent the H-polarization case, while equations (2.1a), (2.1b) and (2.2c) involve E_z, H_r and H_ϕ and represent the E-polarization case. These two sets of equations can be solved independently. The elimination of E_r and E_ϕ from equation (2.1c) gives

$$\frac{1}{r}\frac{\partial}{\partial r}\left(r\frac{\partial H_z}{\partial r}\right) + \frac{1}{r^2}\frac{\partial^2 H_z}{\partial \phi^2} = i\omega\mu k\sigma H_z \tag{2.3}$$

for the H-polarization case, while eliminating H_r and H_ϕ from equation (2.2c) gives

$$\frac{1}{r}\frac{\partial}{\partial r}\left(r\frac{\partial E_z}{\partial r}\right) + \frac{1}{r^2}\frac{\partial^2 E_z}{\partial \phi^2} = i\omega\mu k\sigma E_z \tag{2.4}$$

for the E-polarization case.

If F is used to represent H_z or E_z depending on the case being considered, the same equation may be used for equations (2.3) and (2.4)

$$\nabla^2 F = i\eta^2 F \tag{2.5}$$

where $\eta^2 = \mu k \omega \sigma$.

Since the field quantity $F = f + ig$ is a complex number, equation (2.5) may be written as two equations

$$\nabla^2 f = -\eta^2 g \qquad (2.5a)$$

$$\nabla^2 g = \eta^2 f \qquad (2.5b)$$

Equations (2.5a) and (2.5b) must be solved simultaneously in all regions being considered. In addition, the boundary conditions have to be satisfied.

2.2 The Numerical Method

In the numerical method the conductivity distribution is given over a two-dimensional polar mesh, whose radius is great enough to satisfy the external boundary conditions. An arbitrary part of this grid is shown in Figure 2.

In the present work equations (2.5a) and (2.5b) are replaced by finite difference equations. Any point, except those along the external boundary, can be chosen as point '0'. From equations (2.5a) and (2.5b) we obtain

$$\left(\frac{\partial^2 f}{\partial r^2}\right)_0 + \frac{1}{R}\left(\frac{\partial f}{\partial r}\right)_0 + \frac{1}{R^2}\left(\frac{\partial^2 f}{\partial \phi^2}\right)_0 = -\eta^2 g_0 \qquad (2.6a)$$

$$\left(\frac{\partial^2 g}{\partial r^2}\right)_0 + \frac{1}{R}\left(\frac{\partial g}{\partial r}\right)_0 + \frac{1}{R^2}\left(\frac{\partial^2 g}{\partial \phi^2}\right)_0 = \eta^2 f_0 \qquad (2.6b)$$

Taylor's theorem is used to obtain the corresponding finite difference equations.

$$f_1 = f_0 - \left(\frac{\partial f}{\partial \phi}\right)_0 \Delta\phi_1 + \tfrac{1}{2}\left(\frac{\partial^2 f}{\partial \phi^2}\right)_0 (\Delta\phi_1)^2 - \ldots$$

$$f_2 = f_0 + \left(\frac{\partial f}{\partial r}\right)_0 \Delta r_2 + \tfrac{1}{2}\left(\frac{\partial^2 f}{\partial r^2}\right)_0 (\Delta r_2)^2 + \ldots$$

$$f_3 = f_0 + \left(\frac{\partial f}{\partial \phi}\right)_0 \Delta\phi_3 + \tfrac{1}{2}\left(\frac{\partial^2 f}{\partial \phi^2}\right)_0 (\Delta\phi_3)^2 + \ldots$$

$$f_4 = f_0 - \left(\frac{\partial f}{\partial r}\right)_0 \Delta r_4 + \tfrac{1}{2}\left(\frac{\partial^2 f}{\partial r^2}\right)_0 (\Delta r_4)^2 - \ldots \qquad (2.7)$$

There is a similar set of equations for the g values.

If higher order terms are neglected and finite differences are substituted for the first derivatives, equations (2.6a) and (2.6b) can be written:

$$Af_0 - \eta^2 g_0 = B_1 f_1 + B_2 f_2 + B_3 f_3 + B_4 f_4 \qquad (2.8a)$$

$$Ag_0 + \eta^2 f_0 = B_1 g_1 + B_2 g_2 + B_3 g_3 + B_4 g_4 \qquad (2.8b)$$

where

$$A = \frac{1}{(R\cdot\Delta\phi_1)^2} + \frac{1}{(\Delta r_2)^2} + \frac{1}{(R\cdot\Delta\phi_3)^2} + \frac{1}{(\Delta r_4)^2}$$

$$B_1 = \frac{1}{(R\cdot\Delta\phi_1)^2} + \frac{1}{R^2(\Delta\phi_1 + \Delta\phi_3)}\left(\frac{1}{\Delta\phi_3} - \frac{1}{\Delta\phi_1}\right)$$

$$B_2 = \frac{1}{(\Delta r_2)^2} + \frac{1}{\Delta r_2 + \Delta r_4}\left(\frac{1}{\Delta r_4} - \frac{1}{\Delta r_2} + \frac{1}{R}\right)$$

$$B_3 = \frac{1}{(R\cdot\Delta\phi_3)^2} + \frac{1}{R^2(\Delta\phi_1 + \Delta\phi_3)}\left(\frac{1}{\Delta\phi_1} - \frac{1}{\Delta\phi_3}\right)$$

$$B_4 = \frac{1}{(\Delta r_4)^2} + \frac{1}{\Delta r_2 + \Delta r_4}\left(\frac{1}{\Delta r_2} - \frac{1}{\Delta r_4} - \frac{1}{R}\right)$$

The first derivatives of functions f and g may be approximated by finite differences as above if they vary nearly linearly in the small distances concerned and the adjacent grid spacings do not differ from each other very much.

In the present work the Gauss-Seidel iteration method is employed wherein the most recent values of f and g for the four nearest points surrounding point '0' are used in each step of the iteration to determine the subsequent values of f and g for point '0' (Smith, 1969).

2.3 Internal Boundary Conditions

2.3.1 General

Equations (2.8a) and (2.8b) must be satisfied at point '0' for each of the regions surrounding it. This means that both (2.8a) and (2.8b) represent four equations each since there are four regions of different conductivity around point '0'. These equations in which the first subscript

refers to the conductive region while the second subscript indicates the grid point are written

$$
\begin{aligned}
Af_{10} - \eta_1^2 g_{10} &= B_1 f_{11} + B_2 f_{12} + B_3 \underline{f_{13}} + B_4 \underline{f_{14}} \\
Af_{20} - \eta_2^2 g_{20} &= B_1 \underline{f_{21}} + B_2 f_{22} + B_3 f_{23} + B_4 \underline{f_{24}} \\
Af_{30} - \eta_3^2 g_{30} &= B_1 \underline{f_{31}} + B_2 \underline{f_{32}} + B_3 f_{33} + B_4 f_{34} \\
Af_{40} - \eta_4^2 g_{40} &= B_1 f_{41} + B_2 \underline{f_{42}} + B_3 \underline{f_{43}} + B_4 f_{44}
\end{aligned}
\qquad (2.9a)
$$

$$
\begin{aligned}
Ag_{10} + \eta_1^2 f_{10} &= B_1 g_{11} + B_2 g_{12} + B_3 \underline{g_{13}} + B_4 \underline{g_{14}} \\
Ag_{20} + \eta_2^2 f_{20} &= B_1 \underline{g_{21}} + B_2 g_{22} + B_3 g_{23} + B_4 \underline{g_{24}} \\
Ag_{30} + \eta_3^2 f_{30} &= B_1 \underline{g_{31}} + B_2 \underline{g_{32}} + B_3 g_{33} + B_4 g_{34} \\
Ag_{40} + \eta_4^2 f_{40} &= B_1 g_{41} + B_2 \underline{g_{42}} + B_3 \underline{g_{43}} + B_4 g_{44}
\end{aligned}
\qquad (2.9b)
$$

The underlined values are so-called 'fictitious values' (Jones and Pascoe, 1971) and must be determined from the boundary conditions.

2.3.2 H-polarization

Since the tangential components of $\underline{E}$ are continuous across the boundaries of each conductivity region, the fictitious values of f and g may be expressed in terms of

existing values.

The boundary conditions are

$$(E_r)_1 = (E_r)_2 \qquad (E_\phi)_1 = (E_\phi)_4$$
$$(E_r)_3 = (E_r)_4 \qquad (E_\phi)_2 = (E_\phi)_3 \tag{2.10}$$

and from equations (2.2a) and (2.2b) we obtain

$$F_{11} - F_{10} = \frac{n_1^2}{n_2^2}(\underline{F_{21}} - F_{20})$$
$$F_{10} - \underline{F_{13}} = \frac{n_1^2}{n_2^2}(F_{20} - F_{23})$$
$$\underline{F_{31}} - F_{30} = \frac{n_3^2}{n_4^2}(F_{41} - F_{40})$$
$$F_{30} - F_{33} = \frac{n_3^2}{n_4^2}(F_{40} - \underline{F_{43}})$$

(2.10a)

$$F_{12} - F_{10} = \frac{n_1^2}{n_4^2}(\underline{F_{42}} - F_{40})$$
$$F_{10} - \underline{F_{14}} = \frac{n_1^2}{n_4^2}(F_{40} - F_{44})$$
$$F_{22} - F_{20} = \frac{n_2^2}{n_3^2}(\underline{F_{32}} - F_{30})$$
$$F_{20} - \underline{F_{24}} = \frac{n_2^2}{n_3^2}(F_{30} - F_{34})$$

The fictitious values of $F_{jk} = f_{jk} + ig_{jk}$ may be eliminated in equations (2.9a) and (2.9b). Since $f_{jk} = f_k$ and $g_{jk} = g_k$, after adding the two sets of equations separately we obtain

$$af_0 + bg_0 = c_1f_1 + c_2f_2 + c_3f_3 + c_4f_4 \qquad (2.11a)$$

$$ag_0 - bf_0 = c_1g_1 + c_2g_2 + c_3g_3 + c_4g_4 \qquad (2.11b)$$

where

$$a = 4A + B_1\left(\frac{\eta_2^2}{\eta_1^2} + \frac{\eta_3^2}{\eta_4^2} - 2\right) + B_2\left(\frac{\eta_3^2}{\eta_2^2} + \frac{\eta_4^2}{\eta_1^2} - 2\right) + B_3\left(\frac{\eta_1^2}{\eta_2^2} + \frac{\eta_4^2}{\eta_3^2} - 2\right) + B_4\left(\frac{\eta_1^2}{\eta_4^2} + \frac{\eta_2^2}{\eta_3^2} - 2\right)$$

$$b = -(\eta_1^2 + \eta_2^2 + \eta_3^2 + \eta_4^2)$$

$$c_1 = B_1\left(\frac{\eta_2^2}{\eta_1^2} + \frac{\eta_3^2}{\eta_4^2} + 2\right)$$

$$c_2 = B_2\left(\frac{\eta_3^2}{\eta_2^2} + \frac{\eta_4^2}{\eta_1^2} + 2\right)$$

$$c_3 = B_3\left(\frac{\eta_1^2}{\eta_2^2} + \frac{\eta_4^2}{\eta_3^2} + 2\right)$$

$$c_4 = B_4\left(\frac{\eta_1^2}{\eta_4^2} + \frac{\eta_2^2}{\eta_3^2} + 2\right)$$

In the H-polarization case equations (2.11a) and (2.11b) are solved simultaneously at each interior point of the mesh for f_0 and g_0.

2.3.3 E-polarization

The continuity of the tangential components of $\underline{H}$ across any interface presents the boundary conditions

$$(H_r)_1 = (H_r)_2 \qquad (H_\phi)_1 = (H_\phi)_4$$
$$(H_r)_3 = (H_r)_4 \qquad (H_\phi)_2 = (H_\phi)_3 \tag{2.12}$$

and from equations (2.1a) and (2.1b) we obtain

$$F_{11} - F_{10} = \underline{F_{21}} - F_{20}$$
$$F_{10} - \underline{F_{13}} = F_{20} - F_{23}$$
$$\underline{F_{31}} - F_{30} = F_{41} - F_{40}$$
$$F_{30} - F_{33} = F_{40} - \underline{F_{43}} \tag{2.12a}$$
$$F_{12} - F_{10} = \underline{F_{42}} - F_{40}$$
$$F_{10} - \underline{F_{14}} = F_{40} - F_{44}$$
$$F_{22} - F_{20} = \underline{F_{32}} - F_{30}$$
$$F_{20} - \underline{F_{24}} = F_{30} - F_{34}$$

By substitution of the underlined fictitious values from the boundary conditions into equations (2.9a) and (2.9b) after adding we obtain a pair of equations

$$Af_0 + \frac{b}{4}g_0 = B_1 f_1 + B_2 f_2 + B_3 f_3 + B_4 f_4 \qquad (2.13a)$$

$$Ag_0 - \frac{b}{4}f_0 = B_1 g_1 + B_2 g_2 + B_3 g_3 + B_4 g_4 \qquad (2.13b)$$

where A, b, B_1, B_2, B_3 and B_4 are as before.

In the E-polarization case the values f_0 and g_0 at each interior point are determined from equations (2.13a) and (2.13b) using Cramer's Rule.

2.4 Boundary Conditions at the Surface

2.4.1 H-polarization

In the H-polarization case, it is seen from equations (2.2a) and (2.2b) that H_z is constant everywhere outside the conducting region. Since all components of $\underline{H}$ are continuous across any interface, this implies that all along the surface the value of H_z is constant and equal to its value in the non-conducting upper half-space. The surface of the conducting region then becomes one of the external boundaries for the H-polarization case. Also, the magnetic field is normalized such that H_o = (1.0, 0.0) is the value along this boundary.

2.4.2 E-polarization

In the E-polarization case there is no correspondingly simple boundary condition for E_z. Price (1950) pointed out that the problem is completely determined if the two-dimensional half-space is considered as the limit of a three-dimensional spherical conductor. In this case the ratio of the tangential components of the inducing and induced fields is independent of the conductivity as the radius tends to infinity. Since the inducing field is assumed to be of the same intensity and form over the entire composite conductor, H_r is the same at the surface approaching the external boundaries (Jones and Price, 1970). At these extremities of the mesh H_ϕ is near zero if the boundary is far enough from any discontinuities inside the conductor near the surface. In this region the field configuration may be regarded as that of a uniform conducting half-space and the solution of equation (2.4) is

$$E_z = E_o \exp\left(-\frac{1+i}{\sqrt{2}}\,\eta r \sin\phi\right) \quad \text{for} \quad 0^\circ \leq \phi \leq 180^\circ \qquad (2.14)$$

where E_o is the value of E_z at the surface. From equation (2.1a) we obtain the surface value of H_r

$$H_r = \frac{1-i}{\sqrt{2}}\,\frac{\eta}{\mu\omega}\,E_o \cos\phi \quad \text{for} \quad \phi = 0^\circ\,,\ 180^\circ\,. \qquad (2.15)$$

As r tends to infinity the radial component equals the total value of the magnetic field along the surface and

$$H_r = H_{oR} = - H_{oL} \qquad (2.15a)$$

where the indices R and L refer to the values at the right and left hand sides of the model respectively. From equation (2.15) we obtain the boundary condition for E_z

$$E_{oR}\, \eta_R = E_{oL}\, \eta_L \quad . \qquad (2.15b)$$

The values η_R and η_L are determined by the conductivities at the extremities of the model just inside the conductor. The electromagnetic field is normalized such that $E_{oL} = (1.0, 0.0)$ is taken for the computations.

In the E-polarization case the field values must be calculated for the non-conducting half-space as well as in the interior of the conductor. Equation (2.2c) indicates that H_r is constant at the extremities of the model near the surface in the non-conducting region. E_z here can be determined from equations (2.15) and (2.1a), since all the tangential components of $\underline{E}$ are continuous across any interface.

$$\frac{1}{r} \frac{\partial E_z}{\partial \phi} = - \frac{1+i}{\sqrt{2}} \eta\, E_o \cos \phi \qquad (2.16a)$$

that is,

$$E_z = E_o \left(1 - \frac{1+i}{\sqrt{2}} \eta\, r \sin \phi\right) \quad . \qquad (2.16b)$$

CHAPTER 3 GENERAL DISCUSSION OF THE COMPUTATIONS

3.1 Initial Values for the Iteration

In the H-polarization case equations (2.11a and b) and in the E-polarization case equations (2.13a and b) are simultaneously solved for f and g applying the Gauss-Seidel iteration method (Smith, 1969). The way in which the initial values of the unknown quantities are set over the mesh influences the number of iterations necessary to obtain the final values. If the initial values exhibit the expected variations in the field configuration, the process requires fewer iterations.

In the H-polarization case the initial field values are set using the solution of equation (2.3) in a uniform conducting half-space

$$H_z = H_o \exp\left(-\frac{1+i}{\sqrt{2}} \eta r \sin\phi\right) \quad . \qquad (3.1)$$

H_o is the normalized surface value and η refers to the conducting region where the actual gridpoint is located. If the point is on the boundary of regions of different conductivities, then the average value is used for η .

There is also another way to set the initial values. It is possible to use the appropriate η values in equation (3.1) only at great distances from the discontinuities where the field may be regarded as uniform and to apply a linear

interpolation for η between the external boundaries in the rest of the conducting region. A vertical contact model was studied by setting the initial values in both ways. The number of iterations using the latter set of initial values significantly exceeded the number of iterations using the actual values of η in each region. It is apparent that the sudden changes in the field values near the vertical discontinuity are smoothed by the linear approximation in η and it takes longer to approach the real field configuration.

In the E-polarization case the initial field values are determined from equation (2.14) for the conducting halfspace and from equation (2.16b) for the non-conducting region. In equation (2.16b) the quantities η and E_o represent interpolated values. A linear change across the upper half of the grid is assumed for $(\eta_R - \eta_L)$ as well as for $(E_{oR} - E_{oL})$.

Similarly, as in the H-polarization case there are different ways to set the initial values in the bottom halfspace by choosing η and E_o in equation (2.14). Both of them may be determined using a linear interpolation as in the non-conducting region. Also in the E-polarization a vertical contact model was examined by setting the initial f and g values in different ways. The number of the iterations required to approach the final values is the smallest when the actual η values are used in each grid point and there is

a sudden change in E_o at the discontinuity. The applied E_o values corresponding to equation (2.15b) are

$$E_o = 1 \qquad \text{for} \qquad \eta = \eta_L \tag{3.2a}$$

$$E_o = \frac{\eta_L}{\eta_R} \qquad \text{for} \qquad \eta = \eta_R \tag{3.2b}$$

$$E_o = \frac{1 + \frac{\eta_L}{\eta_R}}{2} \qquad \text{at the discontinuity.} \tag{3.2c}$$

The iteration procedure takes considerably longer when a linear approximation is used either for η or E_o or for both of them.

In other models the initial E_o values are determined from equations (3.2a, b and c). Equation (3.2c) may be used at every gridpoint where η does not equal η_L nor η_R .

3.2 The Grid

The meshes used for the two different polarization cases are illustrated in Figure 4. The grid spacings are variable so that the values $\Delta\phi_i (i = 1,m)$ and $\Delta r_j (j = 1,n)$ may vary. Also, each region of the mesh can have material of different conductivity. To satisfy the boundary conditions there must not be conductivity changes near the surface in the outer Δr regions. Furthermore, in the E-polarization case $\sigma=0$ for $180^o < \phi < 360^o$.

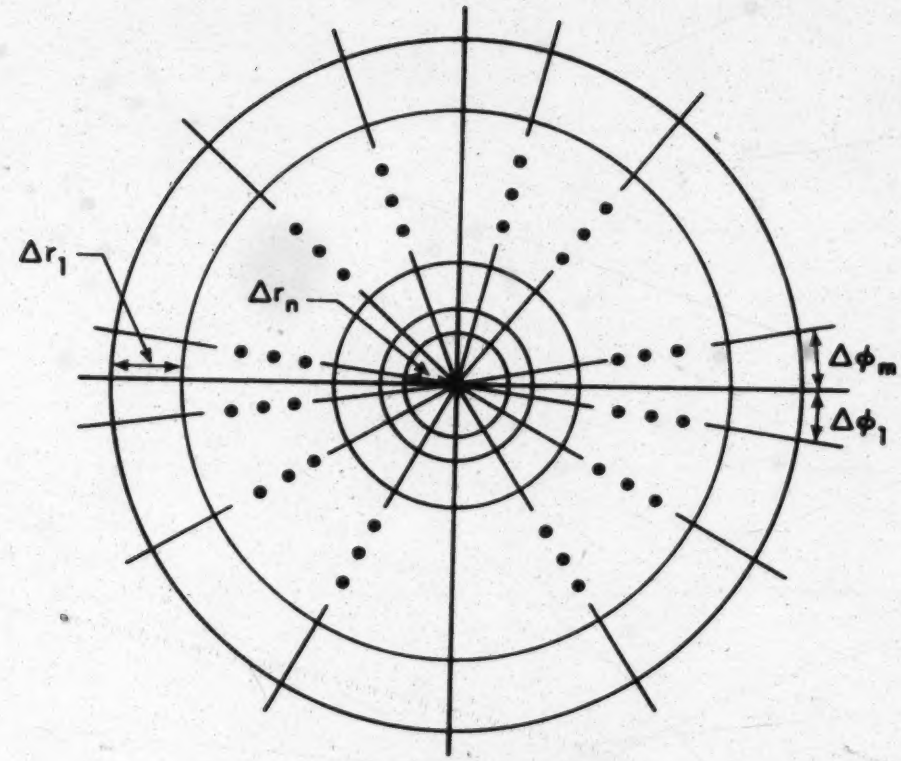

A: E-polarization

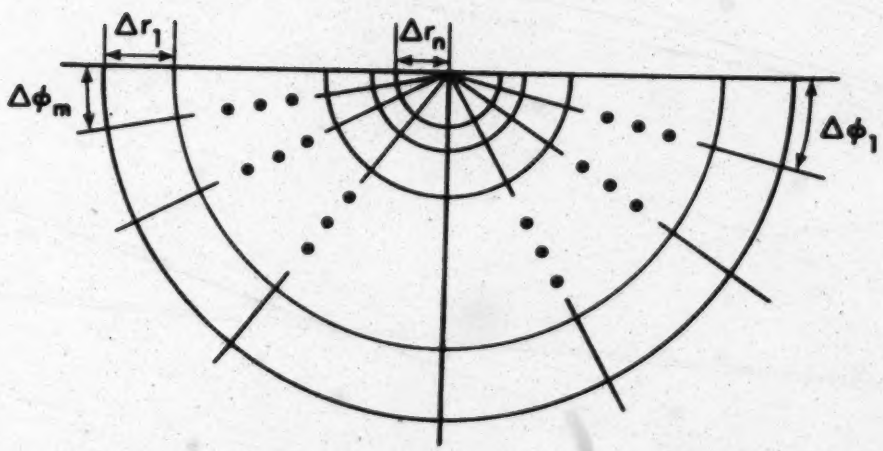

B: H-polarization

Figure 4 The meshes used.

The distance from the origin to the external boundaries ($R_{max} = \sum_{j=1}^{n} \Delta r_j$) is determined for each model considering the skin depths and the conductivity configuration. The skin depth is calculated for each material in the model

$$s = \sqrt{\frac{2}{k\mu\sigma\omega}} \quad . \tag{3.3}$$

The field values along the arc of maximum radius do not change during the iteration procedure. Therefore, the initial values of the iteration must be good approximations of the real field values there. This implies that the external boundary must be far enough from any lateral inhomogeneities near the surface so that the f and g values along the boundary correspond to those above a uniform conductor. Also, if any non-horizontal discontinuity intersects the external boundary of the mesh, the distance of this intersection point from the surface must be large enough so that the field values may be relatively small there. In the case of a uniform conducting half-space the field values are less than about five percent of the surface values in a depth of three times the skin depth. Thus, R_{max} is chosen to be $2 - 3 \times s^*$ depending on the geometrical distribution of the regions of different conductivities where s^* is the skin depth in the material of the highest resistivity in the conducting area.

The grid spacings cannot be chosen arbitrarily for the following reasons:

(1) Some restriction is set for the adjacent grid spacings in the radial as well as in the angular direction by the fact that finite differences are used for the first derivatives of the field quantities in equations (2.6). This implies that Δr_4 must not differ from Δr_2 very much and similarly, $\Delta\phi_1$ has to be nearly as large as $\Delta\phi_3$ (See Figure 2).

(2) The radial distances Δr_2 and Δr_4 may only slightly differ from the lengths of the arcs $R\Delta\phi_1$ and $R\Delta\phi_3$ at each gridpoint. For example, if the grid spacings along the radii are generally much larger than the spacings along the arcs, the iteration proceeds separately to a certain extent for each circle. However, the iteration can be performed correctly even if the ratio of the radial and angular grid spacings cannot be chosen properly. In equations (2.8a and b) the points closest to the point regarded do not have to be used. If the next neighbouring point is still in the same conductivity region, it is possible to take its value or to go even further away from point '0' in Figure 2, if the angular distance $\Delta\phi$ does not considerably increase.

(3) Relatively smaller $\Delta\phi$ values have to be used near the surface to obtain more correct H_r and E_r values along the surface (See section 3.3).

It is not possible to obtain a grid which fills all the above requirements. It is particularly difficult to find the proper ratio for the radius of the smallest arc to the radius of the next arc. If Δr_n is very small, all the $\Delta\phi$ values should be relatively large to fill the second requirement. Also, it is necessary to use a great number of radial grid spacings to set R_{max} large enough so that the first requirement is not violated. In this work Δr_n is chosen to be at least three times as large as Δr_{n-1}. In this way the F value at the central point only slightly influences the values along the arc of smallest radius. The F value at this unique point of the polar grid is taken as the average of the values at the adjacent points on the left and right-hand side after each step of the iteration.

3.3 Calculation of the Surface Values

The surface values of the electric components are calculated using equations (2.2a) and (2.2b) in the H-polarization case. Substituting finite differences for the derivatives we obtain approximate values

$$\text{Ampl } (E_\phi) = \frac{1}{k\sigma}\sqrt{\frac{(\Delta_r f)^2 + (\Delta_r g)^2}{(\Delta r)^2}}$$

$$\text{Phase } (E_\phi) = \arctan\left(\frac{\Delta_r g}{\Delta_r f}\right) \qquad (3.4a)$$

$$\text{Ampl } (E_r) = \frac{1}{k\sigma}\sqrt{\frac{(\Delta_\phi f)^2 + (\Delta_\phi g)^2}{(r \sin \phi_1)^2}}$$

$$\text{Phase } (E_r) = \arctan\left(\frac{\Delta_\phi g}{\Delta_\phi f}\right) \quad . \tag{3.4b}$$

In this case $E_\phi = 0$ all along the surface since $H_o = (1.0,0.0)$ does not change there.

In the E-polarization case the magnetic field values along the surface are determined from equations (2.1a) and (2.1b). Using finite differences again, we obtain

$$\text{Ampl } (H_\phi) = \frac{1}{\mu\omega}\sqrt{\frac{(\Delta_r f)^2 + (\Delta_r g)^2}{(\Delta r)^2}}$$

$$\text{Phase } (H_\phi) = \arctan\left(\frac{-\Delta_r f}{\Delta_r g}\right) \tag{3.5a}$$

$$\text{Ampl } (H_r) = \frac{1}{\mu\omega}\sqrt{\frac{(\Delta_\phi f)^2 + (\Delta_\phi g)^2}{(2r \sin \Delta\phi_1)^2}}$$

$$\text{Phase } (H_r) = \arctan\left(\frac{\Delta_\phi f}{-\Delta_\phi g}\right) \tag{3.5b}$$

$\text{Sin}\Delta\phi_1$ was taken for $\Delta\phi_1$ as if the Cartesian coordinate system were used.

In the E-polarization case the surface values must be corrected by interpolation for the point where the appro-

priate arc intersects the surface. A linear interpolation is used. A region of the mesh near the surface is shown in Figure 3, where

$$\overline{OP}_r = r \cdot \cos(\Delta\phi_1)$$

$$\overline{OP}_\phi = (\overline{OP}_4 + \overline{OP}_2)/2 \qquad (3.6a)$$

$$\overline{OP}_0 = r \quad .$$

The finite differences used in equations (3.5a) and (3.5b) are obtained for the f values

$$\Delta_\phi f = f_{P_3} - f_{P_1}$$

$$\Delta_r f = f_{P_2} - f_{P_4} \qquad (3.6b)$$

and similarly for the g values.

In the H-polarization no interpolation is necessary. E_r values are determined at point P_r by using the values of f and g at point P_3 and at the surface.

The calculation of the surface values from the finite differences implies the assumption that the fields change linearly downward within the conductor. However, the solution of equation (2.5) in any layered conductor is of the form

$$F = D_1 \exp(-\sqrt{i}\,\eta r \sin\phi) + D_2 \exp(\sqrt{i}\,\eta r \sin\phi) \qquad (3.7)$$

where η refers to the actual layer.

If there is no vertical discontinuity near the surface, the upper region of the conducting half-space may be treated as a layered conductor. In a polar mesh the uppermost layer is substituted by the first section of $\Delta\phi$ next to the surface. The thickness of this layer decreases as it approaches the centre of the grid from the outer regions. At the central point it becomes zero and the substitution is not acceptable. Near the extremities of the mesh more accurate results are obtained for the surface values of H_r and E_r by using the exponential approximation rather than the linear one. From equation (3.7) we obtain

$$\frac{\partial F}{\partial \phi} = -\sqrt{i}\, r\eta(D_1 - D_2) \qquad (3.8)$$

where D_1 and D_2 are determined from the field values at the surface and along the radius just under the surface at a distance of $r \cdot \sin\Delta\phi_1$. The value of η taken here is the value of η corresponding to this section. Also

$$E_r = \frac{1}{k\sigma r} \cdot \frac{\partial H_z}{\partial \phi} \qquad (3.9a)$$

$$H_r = \frac{i}{\mu\omega r} \cdot \frac{\partial E_z}{\partial \phi} \qquad (3.9b)$$

If the values of $\Delta_\phi f$ and $\Delta_\phi g$ in equations (3.4b) and (3.5b) are small, more precise results may be obtained using the f and g values at gridpoints that are not those

nearest the surface. However, they must be in a region of the same conductivity. In this case all H_r and E_r values are calculated from the F values along the radius with slope $\Delta\phi^*$ when $\Delta\phi^*$ is larger than $\Delta\phi_1$. Similarly, the surface values of H_ϕ can be determined using greater Δr distances in equation (3.5a).

The apparent resistivity values (Cagniard, 1953) at the surface are calculated from the values of $\underline{E}$ and $\underline{H}$. In the H-polarization case the currents flow perpendicularly to the strike of the two-dimensional model. The apparent resistivity is

$$\rho_r = \frac{k}{\mu} \cdot \frac{1}{\omega} \left(\frac{E_r}{H_z}\right)^2 \quad . \tag{3.10a}$$

In the E-polarization case the currents flow parallel to the strike of the model and the observed resistivity is

$$\rho_z = \frac{k}{\mu} \cdot \frac{1}{\omega} \left(\frac{E_z}{H_r}\right)^2 \quad . \tag{3.10b}$$

The surface values obtained from equations (3.9a and b) differ slightly from those obtained from equations (3.4b) and (3.5b) respectively. The only exceptions are the small slope models in the E-polarization case (See Figure 10). Figure 5 shows the amplitude and phase values of H_r and the amplitudes of the apparent resistivity for the slopes $\tan \alpha_2 = 0.2$ and $\tan \alpha_5 = \infty$. The curves noted by stars are

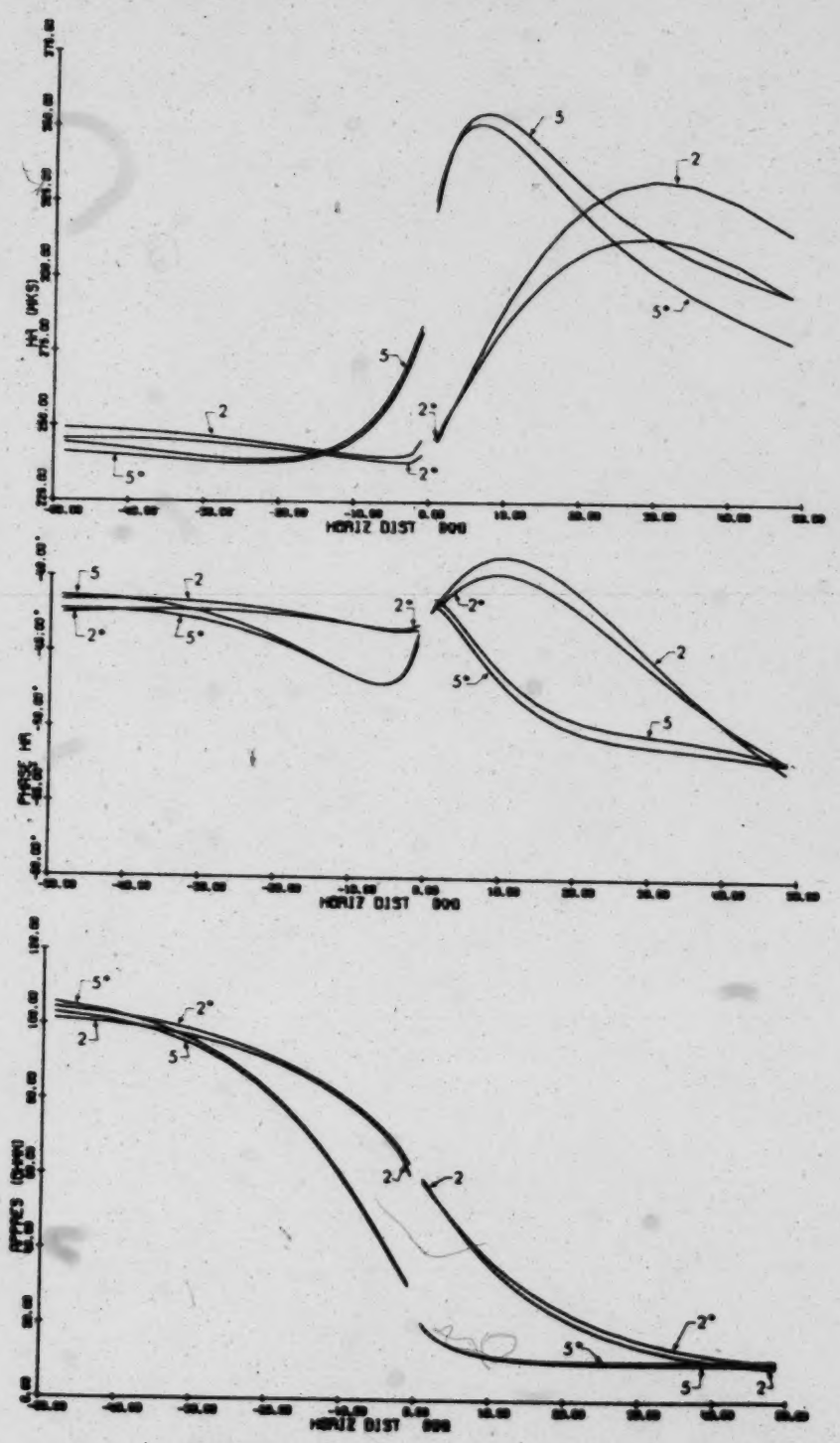

Figure 5 The surface values of H_r and ρ_z for the sloping contact models with $\tan\alpha_2 = 0.2$ (curves 2) and $\tan\alpha_5 = \infty$ (curves 5) in the E-polarization case. The curves marked with stars are calculated from equation (3.5b), the curves without stars from equation (3.9b).

culated from equation (3.5b) while those without stars from equation (3.9b). The differences between the corresponding values increase at the extremities of the surface. Near the central point the two curves deviate from each other for the smaller slope only. Curves 2 and 2^* show, especially for the apparent resistivity, that the exponential approximation does not work as well as the linear approximation for this particular model. Over the model of the vertical contact, however, there is no observable difference between curves 5 and 5^* in the central region. In the H-polarization case the E_r values for all slopes determined from equation (3.9a) are acceptable as well as the values from equation (3.4b).

3.4 The Iteration Procedure

As it was mentioned in sections 2.2 and 3.1, the calculation of the unknown field values employs the Gauss-Seidel iteration method. After the initial values over the mesh are set, the iteration procedure continues until all the differences between the most recently calculated f_0 and g_0 values in equations (2.11a and b) or (2.13a and b) and the corresponding values from the previous step of the iteration are less than a given residual ε . For each model

the value of ε is taken as 0.0001 . This is 0.01 percent of the normalized f value at the surface on the left-hand side of the model.

The point-by-point iteration proceeds in a clockwise direction around the arcs of the mesh, beginning with the outermost circle and moving inward. Since in each step of this procedure the most recent available values of f and g are used at the four neighbouring points around the point regarded, some degree of asymmetry is shown by the final field values even if the conductivity configuration is symmetrical (See section 4.3).

Such asymmetry is investigated for the sloping contact models. In the H-polarization case the slopes with $\tan \alpha_1 = 0.1$ and $\tan \alpha_5 = \infty$ are studied. The slopes with $\tan \alpha_2 = 0.2$ and $\tan \alpha_5 = \infty$ are considered for the E-polarization case. Initially the region of higher conductivity is placed on the right-hand side of the model as is shown in Figure 10. Afterward this region is shifted to the left-hand side of the mesh. These two configurations will be referred to as the 'original' and 'image' model respectively. The standard clockwise direction for the iterations around the arcs of the mesh implies that in the two cases the iteration proceeds in the opposite direction

with respect to the different positions of the better conductor. The radial direction of the iteration is the same for both models.

The final grid values at the corresponding grid-points of the two configurations which are images of each other deviate from one another for each slope. These differences are much larger in the E-polarization case than in the H-polarization case since in the latter case the iteration proceeds over a mesh whose arcs are half circles only (See Figure 4). The maximum differences between the field values obtained from the 'original' and the 'image' configurations are observed in the central regions of the meshes.

	E-polarization	H-polarization
Maximum differences in f:		
small slope	0.0082	0.0007
vertical contact	0.0090	0.0026
Maximum differences in g:		
small slope	0.0042	0.0004
vertical contact	0.0034	0.0013

The relative differences in the f values near the surface are less than 0.04 percent of the f values at the

corresponding points in the H-polarization case and less than 1 percent in the E-polarization case. The relative differences in the g values are much larger. Although in the investigated cases they are under 18 percent of the corresponding g values at the points near the surface, in other cases this value may be exceeded since g values are near zero close to the surface.

The differences described above are negligible with respect to the surface values of E_z in the E-polarization case and H_z in the H-polarization case. However, the surface values of the other field components calculated over the 'original' models exhibited in Figure 10 deviate from the corresponding values determined for the 'image' models. For the purpose of comparison the profiles for the 'image' models are reversed in Figures 6 and 7.

Figure 6 shows the surface values of the electric field for the two slopes investigated in the H-polarization case. The amplitude and phase values of E_r are calculated from equation (3.9a). Above the poor conductor and moving toward the central point the curves determined from the two different configurations deviate from each other for both slopes.

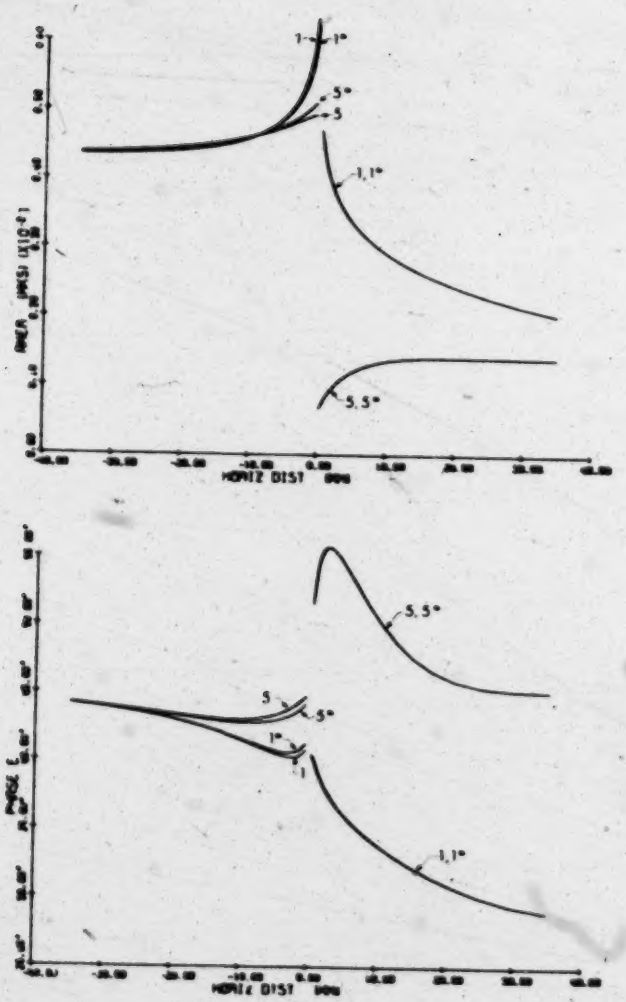

Figure 6 The surface values of E_z for the sloping contact models with $\tan \alpha_1 = 0.1$ (curves 1) and $\tan \alpha_5 = \infty$ (curves 5) in the H-polarization case. The curves marked with stars are determined from the 'image' model and the curves without stars from the 'original' model as explained in section 3.4.

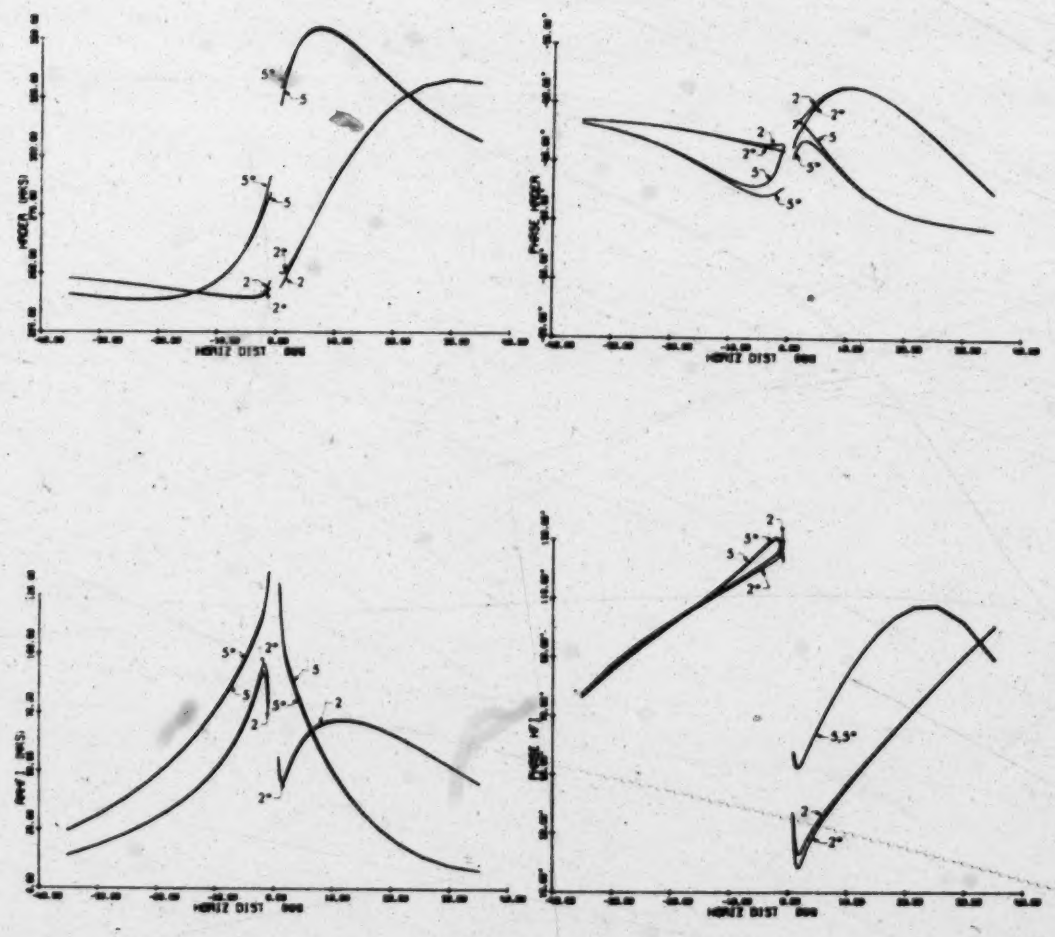

Figure 7 The surface values of H_r and H_ϕ for the sloping contact models with $\tan\alpha_2 = 0.2$ (curves 2) and $\tan\alpha_5 = \infty$ (curves 5) in the E-polarization case. The curves marked with stars are determined from the 'image' model and the curves without stars from the 'original' model as explained in section 3.4.

Figure 7 exhibits the surface values of the magnetic field components for the two slopes examined in the E-polarization case. The amplitude and phase values of H_r and H_ϕ are calculated from equations (3.9b) and (3.5a) respectively. The differences between the profiles determined from the 'original' and the 'image' models increase for the H_r component moving toward the central point from both sides for both slopes. H_r values determined from equation (3.5b) would show the same features. The H_ϕ profiles differ only slightly from each other above the vertical contact, but there is some deviation between the curves from the different models for the small slope, especially in the phase values. It is apparent that the H_ϕ values change less when the direction of the iteration is changed around the arcs only, since they are determined from the field values along the radii.

CHAPTER 4 RESULTS FROM THREE TWO-DIMENSIONAL MODELS

4.1 General Description of the Results

The perturbation problem was studied for three different two-dimensional models using the described method in the cylindrical co-ordinate system. The models are illustrated in Figures 8, 9 and 10. The first two models, the ridge and the dyke, are symmetric while the five different slopes in the third model show asymmetric conductivity configurations.

Both H and E-polarization cases are investigated for each model. The mesh used in the H-polarization corresponds to the bottom half of the mesh used in the E-polarization for each model. The grid spacings applied in the individual cases are presented in Table 1-4 and will be discussed later.

The field values are calculated throughout the whole region of the grid. In general

$$F = (f + ig)\exp(i\omega t) \qquad (4.1)$$

where $F = H_z$ or $F = E_z$ depending on the case being considered. The amplitude of the field is determined at each gridpoint

$$\text{Ampl}(F) = \sqrt{f^2 + g^2} \quad . \qquad (4.2)$$

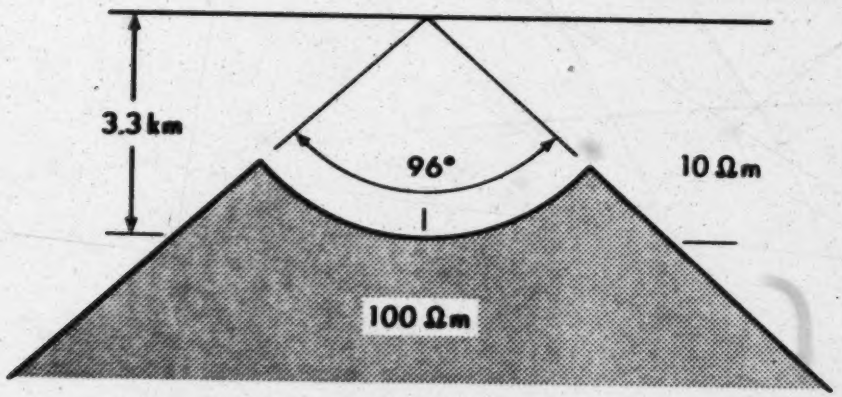

Figure 8 The ridge model.

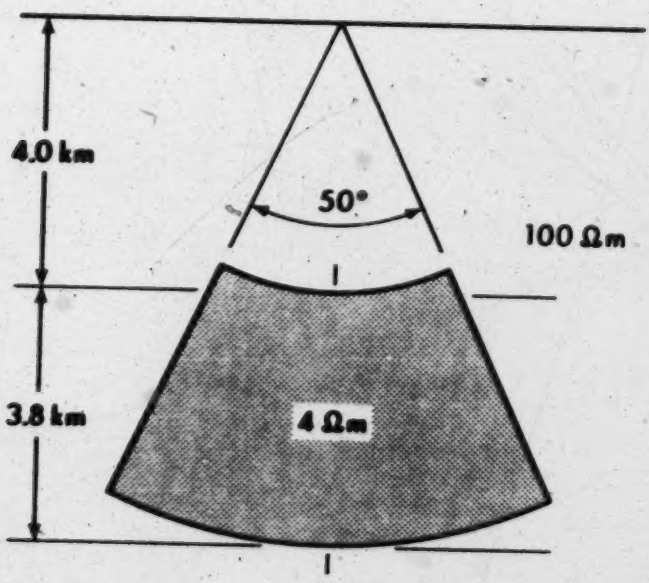

Figure 9 The dyke model.

tan α_1 = 0.1

tan α_3 = 0.5

tan α_2 = 0.2

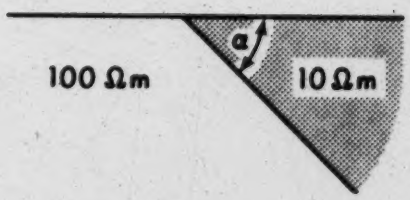

tan α_4 = 1.0

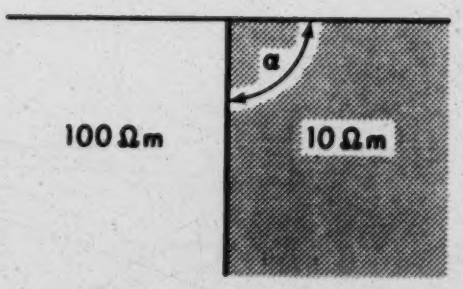

tan α_5 = ∞

Figure 10 The sloping contact models.

The amplitude distribution of the magnetic or electric field depending on the polarization case is presented over a limited region of the mesh where the inhomogeneities are located for each model at each frequency investigated. According to equation (2.1c) in the H-polarization case, the contours of equal H_z represent the lines of force of the electric field and consequently the lines of current flow perpendicular to the strike of the two-dimensional model. In the E-polarization case, equation (2.2c) shows that the contours of equal E_z correspond to the lines of force of the magnetic field. Also, after multiplying by the conductivities of the corresponding regions of the model, these contours represent the distribution of the current density flowing parallel to the strike of the structure.

The instantaneous field values observed are calculated from equation (4.1)

$$F_{obs} = Re[F] = f \cos(\omega t) - g \sin(\omega t) \quad . \qquad (4.3)$$

For each model the field configuration is presented for certain epochs of the first half of the oscillation period $T = 2\pi/\omega$ over a region where the uniform source field is mostly perturbed. During the cycle the source field changes direction. The configuration of the induced electric currents

is the same at time t = 0 as at t = T/2 except for the direction of the currents. During the second half of the period the currents flow in the direction opposite to that of the first half.

In the H-polarization case the surface values of the horizontal electric field and the apparent resistivity from equation (3.10a) are presented. The profile of the amplitude of ρ_r is similar to that of E_r since H_z is constant along the surface. It is sufficient to exhibit only the phase profile of E_r . In the E-polarization case the surface values of the electric field and the horizontal and vertical magnetic components are determined. Also, the apparent resistivity from equation (3.10b) and the ratio of the two magnetic field components are presented.

Since in the E-polarization case the electric field and in the H-polarization case the magnetic field is normalized, the other field components calculated from these normalized $\underline{E}$ and $\underline{H}$ values show relative values. The apparent resistivities represent real values.

The computer programs work in electromagnetic as well as in MKS units. The calculations are done in MKS units for each model except for the dyke model.

E_r and H_r values are calculated using the linear as well as the exponential approximation as explained in

section 3.3 . The values of D_1 and D_2 in equation (3.8) are determined from the F values along the surface and along the radius whose vertical distance from the surface is $r \cdot \sin\Delta\phi$ where $\Delta\phi$ is 2.5^o - 3.5^o . Since more correct surface values are obtained from the exponential approximation in the outer region of the mesh and the results of the two approximations do not observably differ from each other near the central point in most cases considered, the profiles presented in this chapter are determined from equation (3.9a) or (3.9b) depending on the polarization case. The only exception is the sloping contact model in the E-polarization case as discussed in section 3.3 .

Each of the profiles shows a gap above the central point of the mesh. There are two reasons for not retaining the values there. (1) The central point is in a special position. The field values there may be determined using a Cartesian co-ordinate system. However, these values usually do not fit the corresponding profiles since they are calculated from gridpoints whose positions relative to the central point are quite different from the relation between the points of the polar mesh. (2) The radius of the innermost arc is at least three times as large as the grid spacing between this arc and the next one. In this way the substitution of finite differences in equations (2.6) is only approxi-

mate for the points around the circle of smallest radius. This may distort the field values over an even larger region.

Since other authors have published profiles in the Cartesian co-ordinate system, the directions of the radial and angular field components are corrected here so that E_r and H_r are directed to the right and H_ϕ downward all along the surface.

4.2 The Ridge Model

4.2.1 General

A ridge-like model with resistivity 100Ωm surrounded by a material of 10Ωm as shown in Figure 8 is studied. The top of the structure at its center is at a depth of 3.3 km. The perturbation problem is investigated for two different oscillation periods of the source, 10 sec and 100 sec. The skin depth in the covering layer is 5.03 km for the shorter period and 15.92 km for the longer period. The sets of grid spacings used in the mesh are given in Table 1. The radius of the outermost arc of the mesh is 68.7 km for the 10 sec period and 155.3 km for the 100 sec period. The calculations are done in MKS units.

Table 1

Grid Spacings for the Ridge Model

(The radial grid spacings are in kms from the central point toward the external boundary, while the angular grid spacings are in degrees in a clockwise direction beginning at the surface on the right-hand side of the model)

Δr set for T = 10 sec:

.35, .1, .12, .14, .17, .2, .24, .28, .32, .37, .46, .55, .67,

.8, .95, 1.15, 1.43, 1.6, 1.8, 2.1, 2.4, 2.8, 3.2, 3.6, 4.,

4.4, 4.5, 5., 5., 5., 5., 5., 5.

Δr set for T = 100 sec:

.4, .1, .13, .17, .22, .28, .35, .42, .53, .7, .8, .95, 1.15,

1.35, 1.55, 1.85, 2.2, 2.55, 2.9, 3.4, 3.9, 4.5, 5.3, 6.1, 7.,

8., 9., 10., 11., 12., 13., 14., 14.5, 15.

$\Delta\phi$ set for both of the oscillation periods:

3, 4, 5, 6, 6, 6, 6, 6, 6, 6, 6, 6, 6, 6, 6, 6,

6, 6, 6, 6, 6, 6, 6, 6, 6, 6, 6, 6, 6, 5, 4, 3

3, 4, 5, 6, 6, 6, 6, 6, 6, 6, 6, 6, 6, 6, 6, 6,

6, 6, 6, 6, 6, 6, 6, 6, 6, 6, 6, 6, 6, 5, 4, 3

4.2.2 H-polarization

Figure 11 shows the amplitude contours of H_z for both oscillation periods studied. It can be seen that the currents are concentrated above the ridge. Inside the lower conductivity structure the current lines spread downward. This tendency is better observed for the shorter period since the skin depth is less.

The instantaneous field configurations for the 10 sec oscillation period are illustrated in Figure 13. At the beginning of the period there are strongly curved negative current lines above the sloping sides of the ridge well below the surface. During the first quarter of the oscillation period the currents penetrate deeper into the conductor. The current lines near the surface on the left-hand side become separated from those on the right-hand side. At the beginning of the second quarter-cycle the currents are mainly concentrated above the sides of the ridge in the better conductor. During this quarter-cycle the curved current lines move downward and decay and currents of opposite direction increase near the surface.

Figure 14 shows the surface values of the electric field and the apparent resistivity. The profiles feature similar changes for the two different oscillation periods. However, the increase in the E_r and ρ_r values toward the

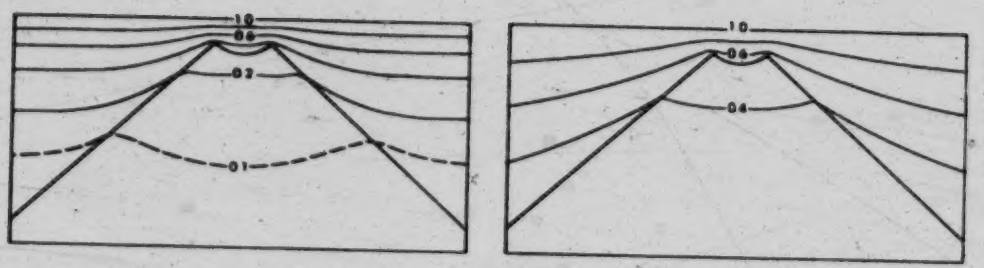

A: T = 10 sec. B: T = 100 sec.

Figure 11 Ridge model, H-polarization. Amplitude contours of H_z.

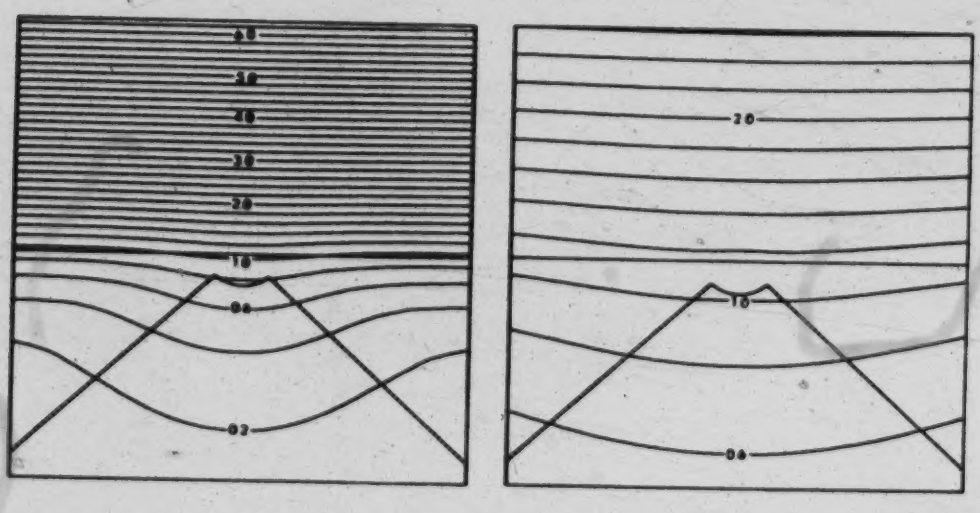

A: T = 10 sec. B: T = 100 sec.

Figure 12 Ridge model, E-polarization. Amplitude contours of E_z.

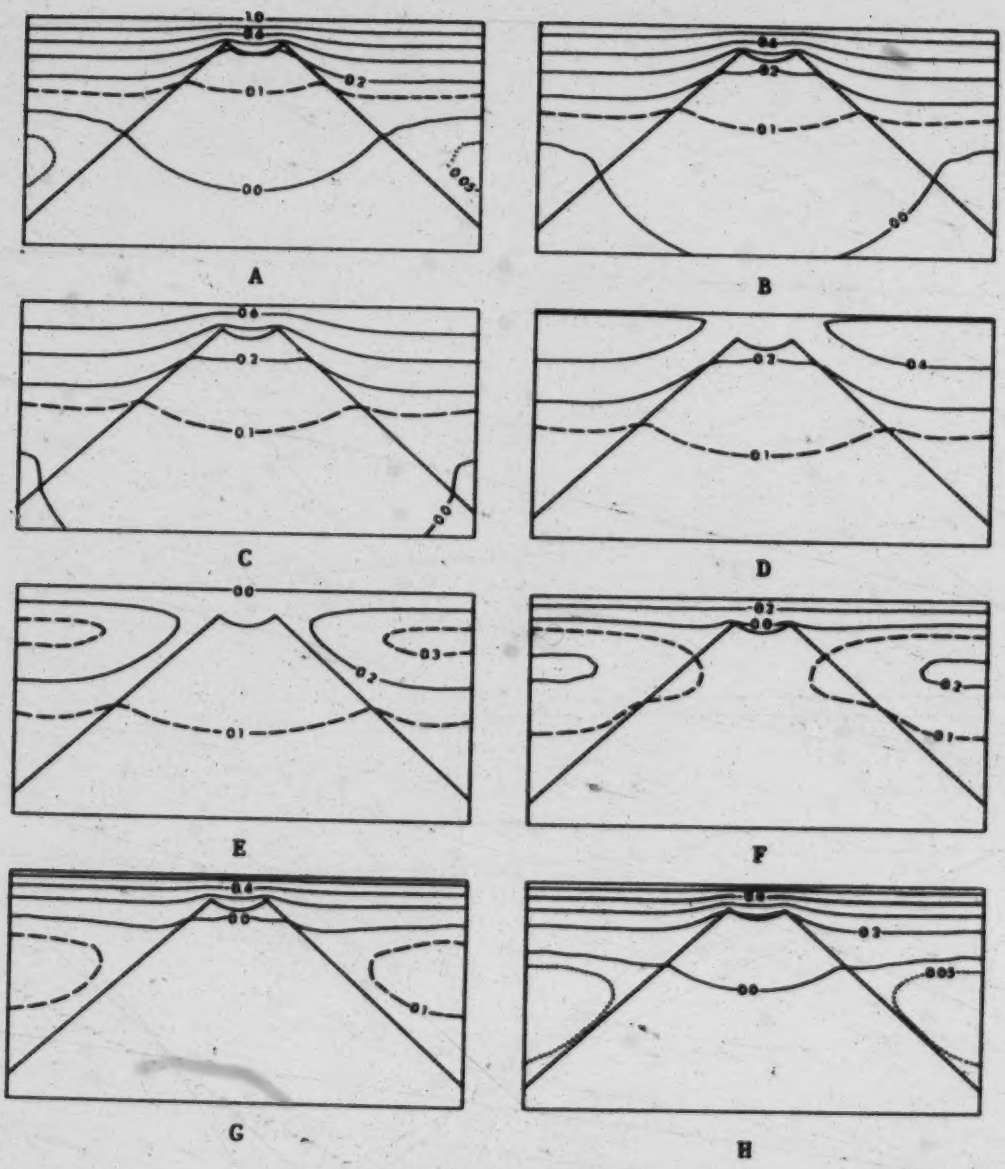

Figure 13 Ridge model, H-polarization. Contours of equal H_z at equal intervals of one-sixteenth of the period. (T = 10 sec)

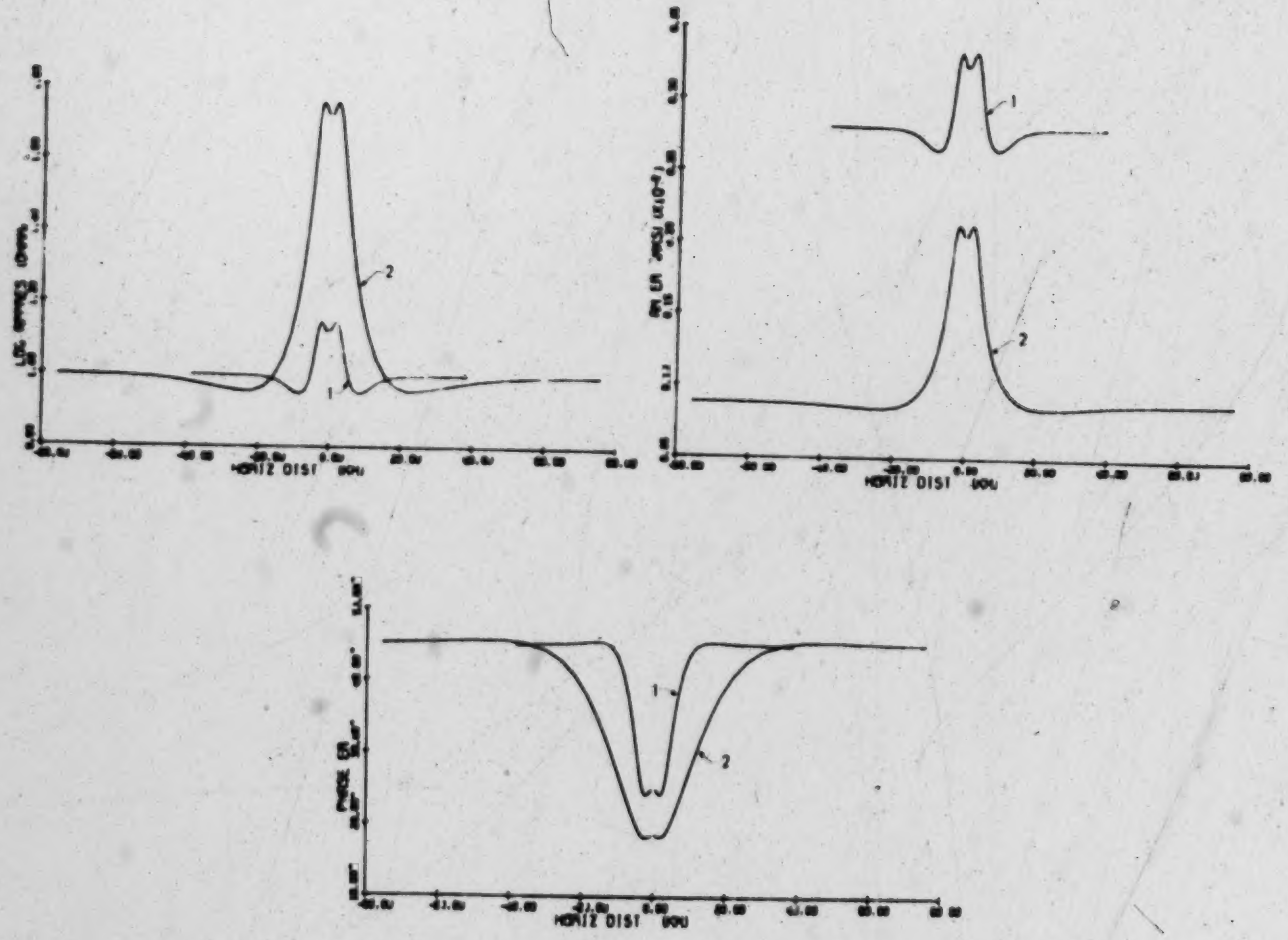

Figure 14 Ridge model, H-polarization. Amplitude and phase profiles of E_x and ρ_a. Curves 1: T = 10 sec; curves 2: T = 100 sec.

central point is larger for the longer period since a greater proportion of the currents penetrates into the region of higher resistivity. There is a small dip in the curves above the top of the ridge for both periods. The maxima are located slightly nearer the central point than the top edges of the ridge. These maxima occur at the places where the density of the current lines is greatest. Above the middle of the ridge the E_r and correspondingly the ρ_r values decrease since the higher conductivity layer is thicker there. The profiles correspond to those of a uniform field outside a distance of 20 km from the center for the 10 sec period and 50 km for the 100 sec period.

4.2.3 E-polarization

Figure 12 shows the amplitude contours of E_z for both oscillation periods studied. It is apparent for the shorter period that the density of the currents flowing perpendicularly to the plane considered is much higher above the slopes of the ridge than inside it, especially when the different conductivities are taken into account.

The instantaneous field values at eight successive epochs during half of the cycle are presented in Figures 15 and 16 for the 10 sec oscillation period. At the end of the first quarter of the period the region of maximum current

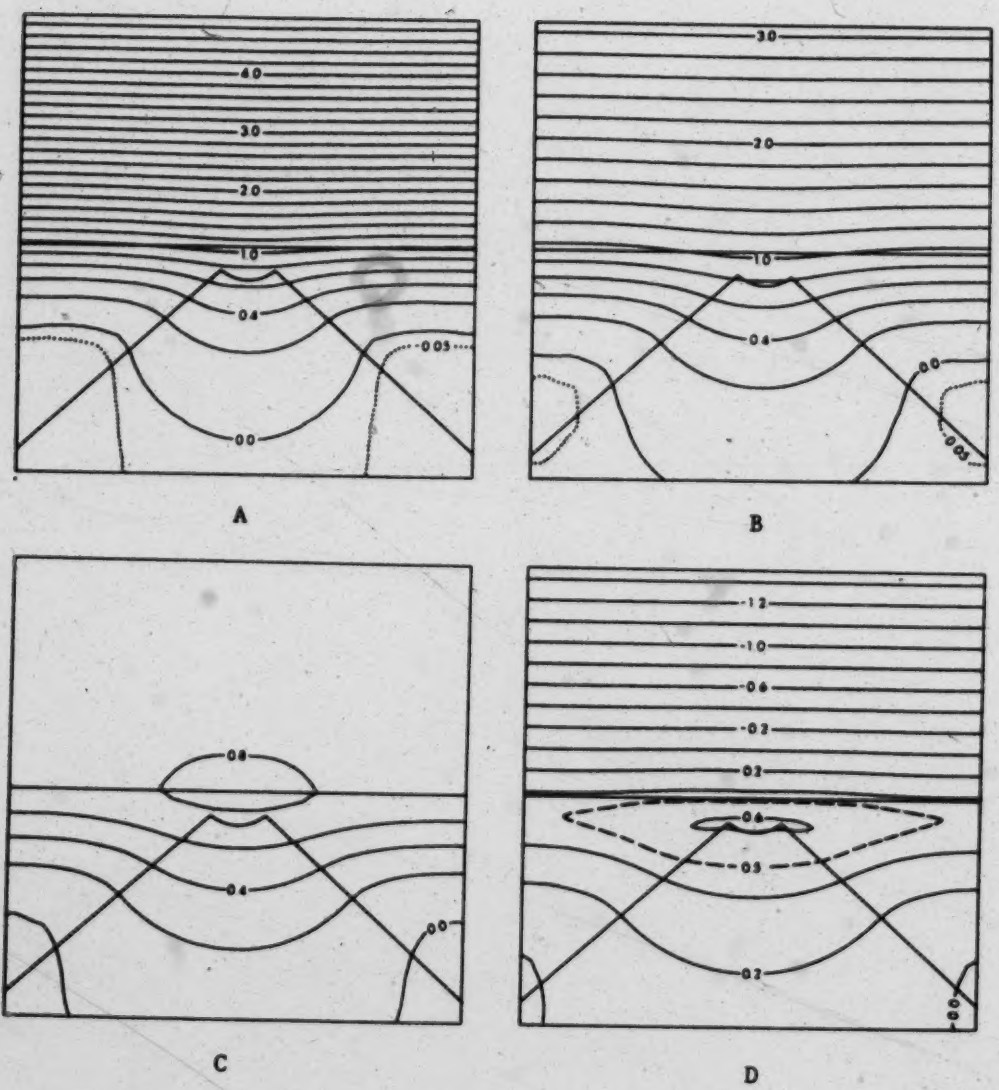

Figure 15 Ridge model, E-polarization. Contours of equal E_x at equal intervals of one-sixteenth of the period for the first four epochs. (T = 10 sec)

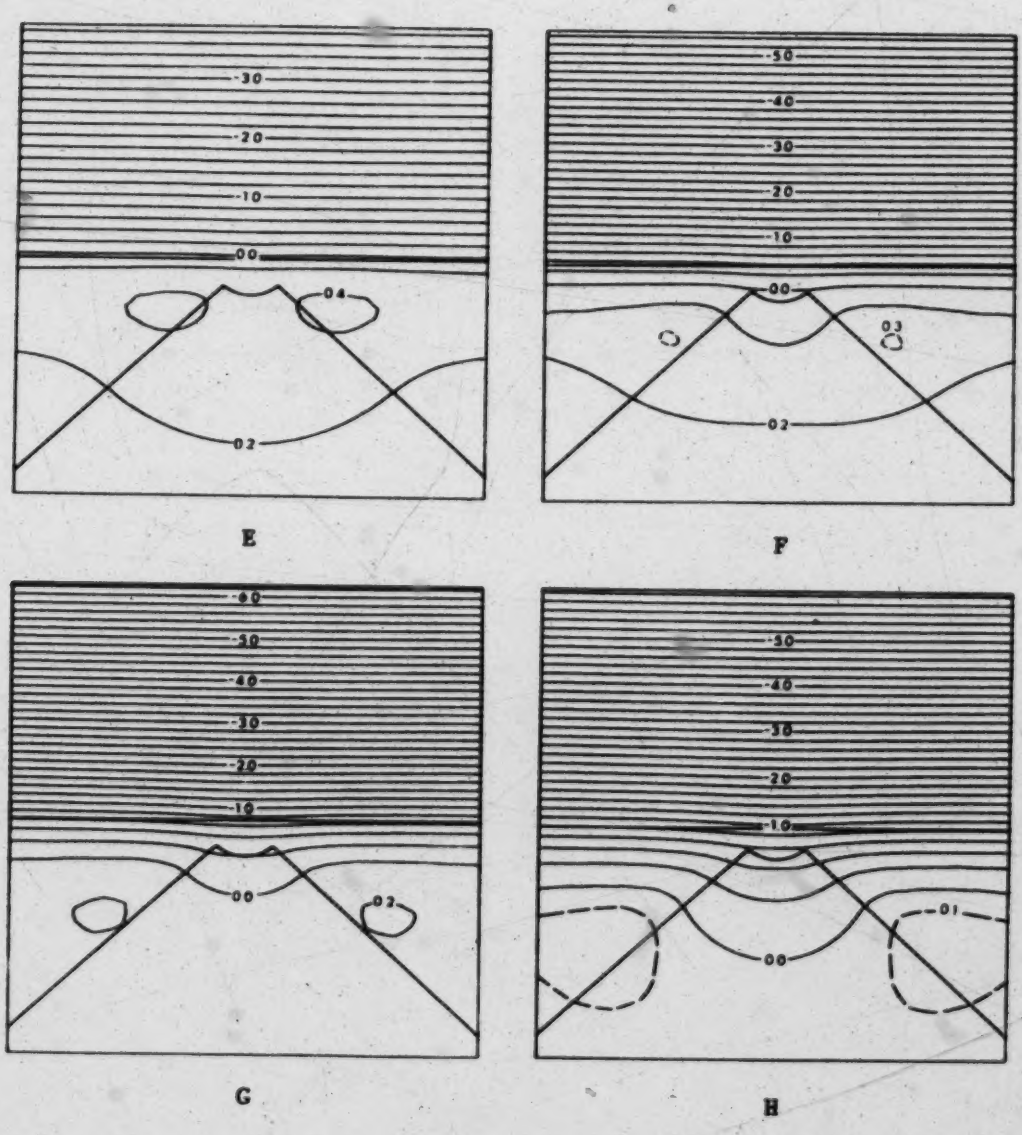

Figure 16 Ridge model, E-polarization. Contours of E_x at equal intervals of one-sixteenth of the period for the second four epochs. (T = 10 sec)

density lies directly above the ridge. During the second quarter of the period this current concentration divides into two parts and separate current wedges are formed above the slopes of the structure. These current concentrations move downward and decrease in intensity with time while the field increases in the opposite direction near the surface.

Figures 17 and 18 exhibit the surface values of the fields. The electric field values increase above the ridge. The maximum is flat and narrow for the shorter period. However, for the longer period there is a dip above the top of the structure and the maxima are approximately above the edges of the ridge. In this latter case the currents penetrate more deeply into the higher resistivity region. There are large maxima in the H_ϕ values on each side of the structure for both periods, but these occur farther from the center of the structure for the longer period since the skin depth is larger. Also, for the longer period, some small secondary maxima appear near the central point. Since the ridge is symmetric, H_ϕ is zero above the middle of the structure and changes sign there. Furthermore, the amplitudes of H_r decrease smoothly approaching the central point and the apparent resistivity profiles show similar features to E_z. The curves of the ratio of the

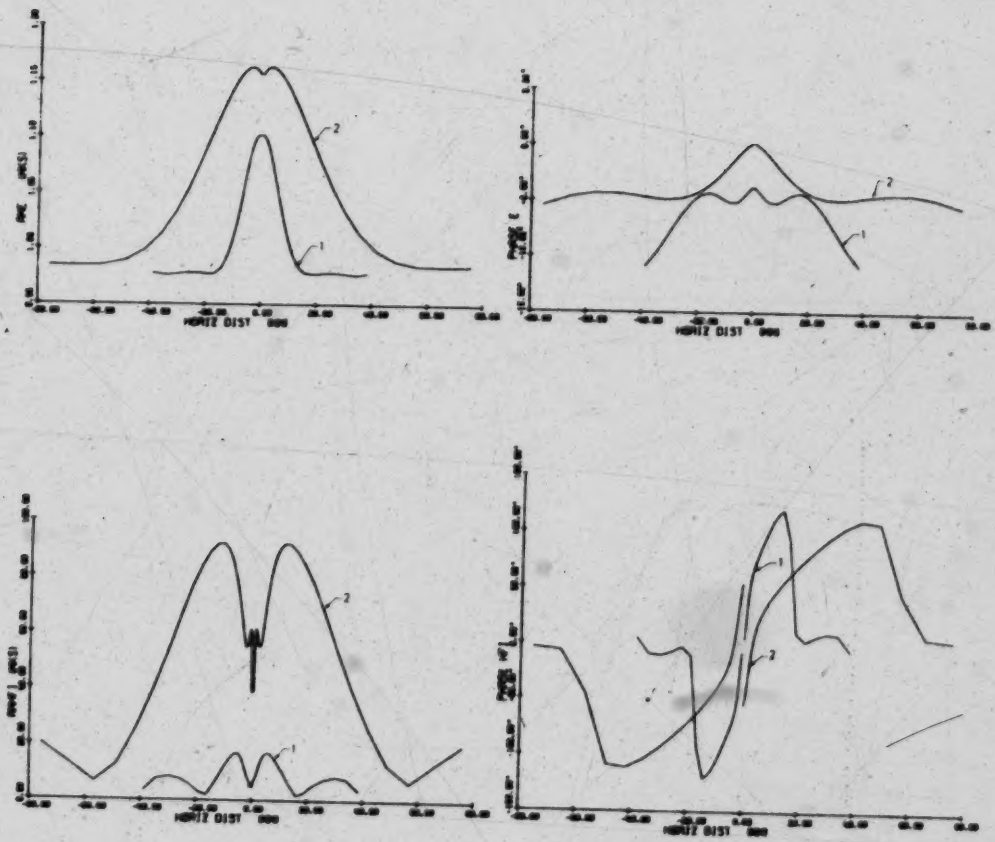

Figure 17 Ridge model, E-polarization. Amplitude and phase profiles of E_z and H_ϕ. Curves 1: T = 10 sec; curves 2: T = 100 sec.

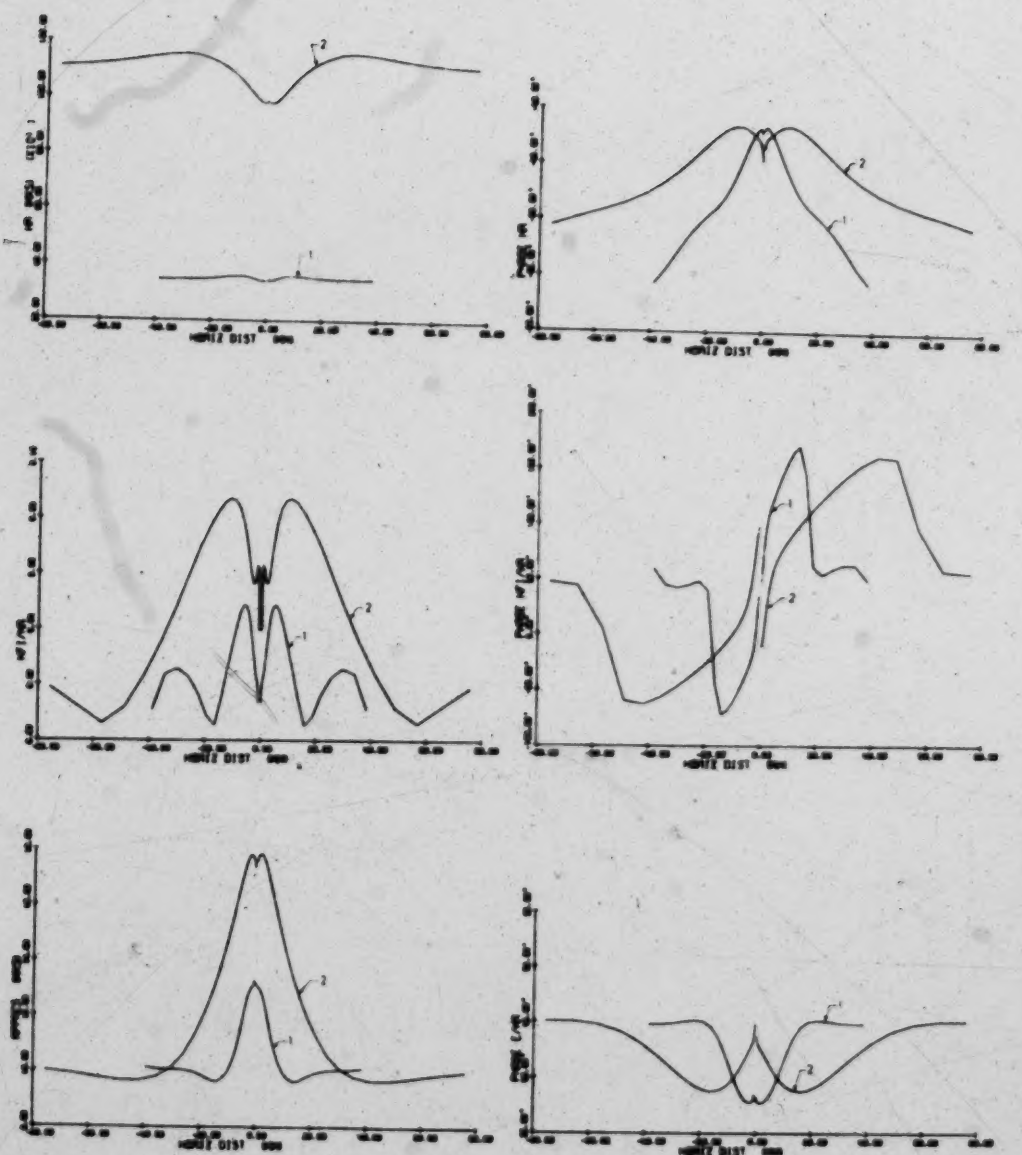

Figure 18 Ridge model, E-polarization. Amplitude and phase profiles of H_x, H_y/H_x and ρ_a. Curves 1: T = 10 sec; curves 2: T = 100 sec.

magnetic components are similar to those of H_ϕ. The apparent resistivity profiles correspond to those of a uniform field outside a distance of about 30 km from the center for the shorter period and 70 km for the longer period. This implies that the ridge affects the field configuration in a larger region in the E-polarization case than in the H-polarization.

4.3 The Dyke Model

4.3.1 General

A dyke-like structure with resistivity 4Ωm buried in a material of 100Ωm as shown in Figure 9 is investigated. The top of the 3.8 km thick structure at its center is at a depth of 4 km. The problem is studied for two different oscillation periods. For the 10 sec period the skin depth is 15.9 km in the poor conductor and 3.2 km in the better conductor. For the 40 sec period the skin depths are 31.8 km and 6.4 km respectively. The grid spacings used are presented in Table 2. The radius of the outermost arc of the mesh is 64.6 km for the shorter period and 109.9 km for the longer period. The calculations are done in electromagnetic units where the resistivities are 4×10^{11} emu and 10^{13} emu.

Table 2

Grid Spacings for the Dyke Model

(The radial grid spacings are in kms from the central point toward the external boundary, while the angular grid spacings are in degrees in a clockwise direction beginning at the surface on the right-hand side of the model)

Δr set for T = 10 sec:

.3, .1, .11, .13, .15, .18, .22, .27, .33, .41, .5, .6, .7,
.8, .9, 1., 1.1, 1.4, 1.6, 1.8, 2.1, 2.4, 2.8, 3.2, 3.6, 4.,
4.4, 4.5, 5., 5., 5., 5., 5.

Δr set for T = 40 sec:

.3, .1, .11, .13, .15, .18, .22, .27, .34, .4, .5, .6, .7,
.8, .9, 1., 1.1, 1.35, 1.6, 1.85, 2.2, 2.6, 3.1, 3.7, 4.4,
5.2, 6.1, 7., 8., 9., 10., 12., 12., 12.

$\Delta\phi$ set for both of the oscillation periods:

3, 4, 5, 6, 6, 6, 6, 6, 6, 6, 6, 5, 5, 5, 5, 5, 5,
5, 5, 5, 5, 5, 5, 6, 6, 6, 6, 6, 6, 6, 6, 5, 4, 3,
3, 4, 5, 6, 6, 6, 6, 6, 6, 7, 7, 7, 7, 7, 7,
7, 7, 7, 7, 7, 7, 6, 6, 6, 6, 6, 6, 5, 4, 3

4.3.2 H-polarization

Figure 19 shows the amplitude contours of H_z for both periods studied. The effect of the dyke is greater for the shorter period since the skin depth is less and the current is denser in the region of the structure. Even for the longer period the concentration of the current lines by the dyke whose conductivity is higher than that of the surrounding material is observed.

The contours of equal H_z at different epochs of the 10 sec oscillation period are exhibited in Figure 21. The current lines are strongly refracted at the boundaries of the structure. During the first quarter of the period positive currents decrease and finally current vortices form in the better conducting region. During the second quarter negative currents increase near the dyke.

The surface values of E_r and ρ_r in Figure 22 show the asymmetry which was discussed in section 3.4. This is observed particularly for the longer oscillation period. There is a slight difference between the two periods in the apparent resistivity profiles. Outside a distance of about 20 km from the center the effect of the dyke is not observed. E_r and ρ_r values show some increase above the structure for the longer period. Also, minima are evident just above the dyke. The distance between these minima is less than the

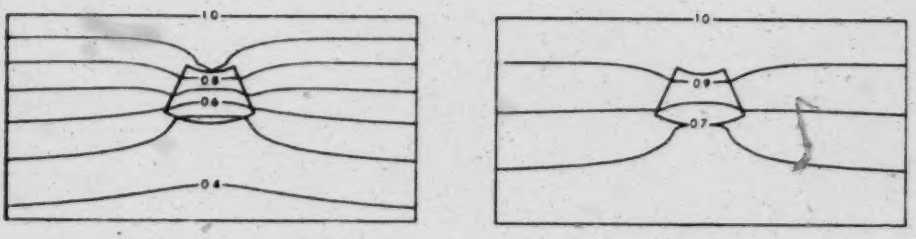

A: T = 10 sec. B: T = 40 sec.

Figure 19 Dyke model, H-polarization. Amplitude contours of H_z.

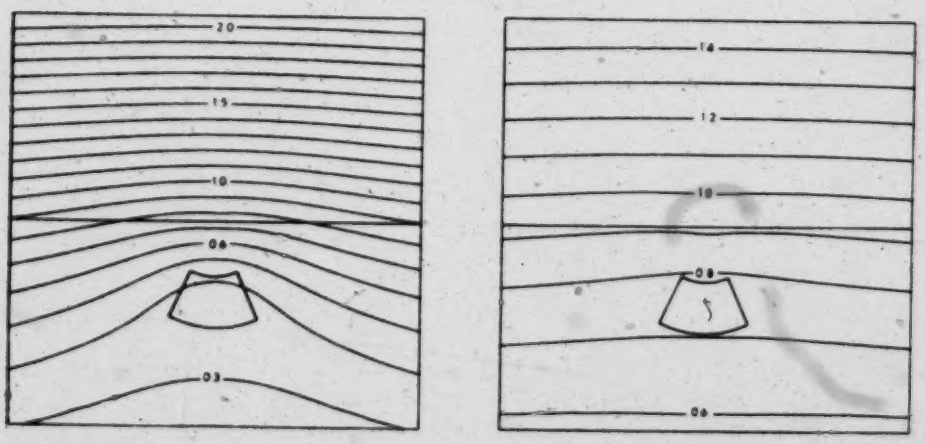

A: T = 10 sec. B: T = 40 sec.

Figure 20 Dyke model, E-polarization. Amplitude contours of E_z.

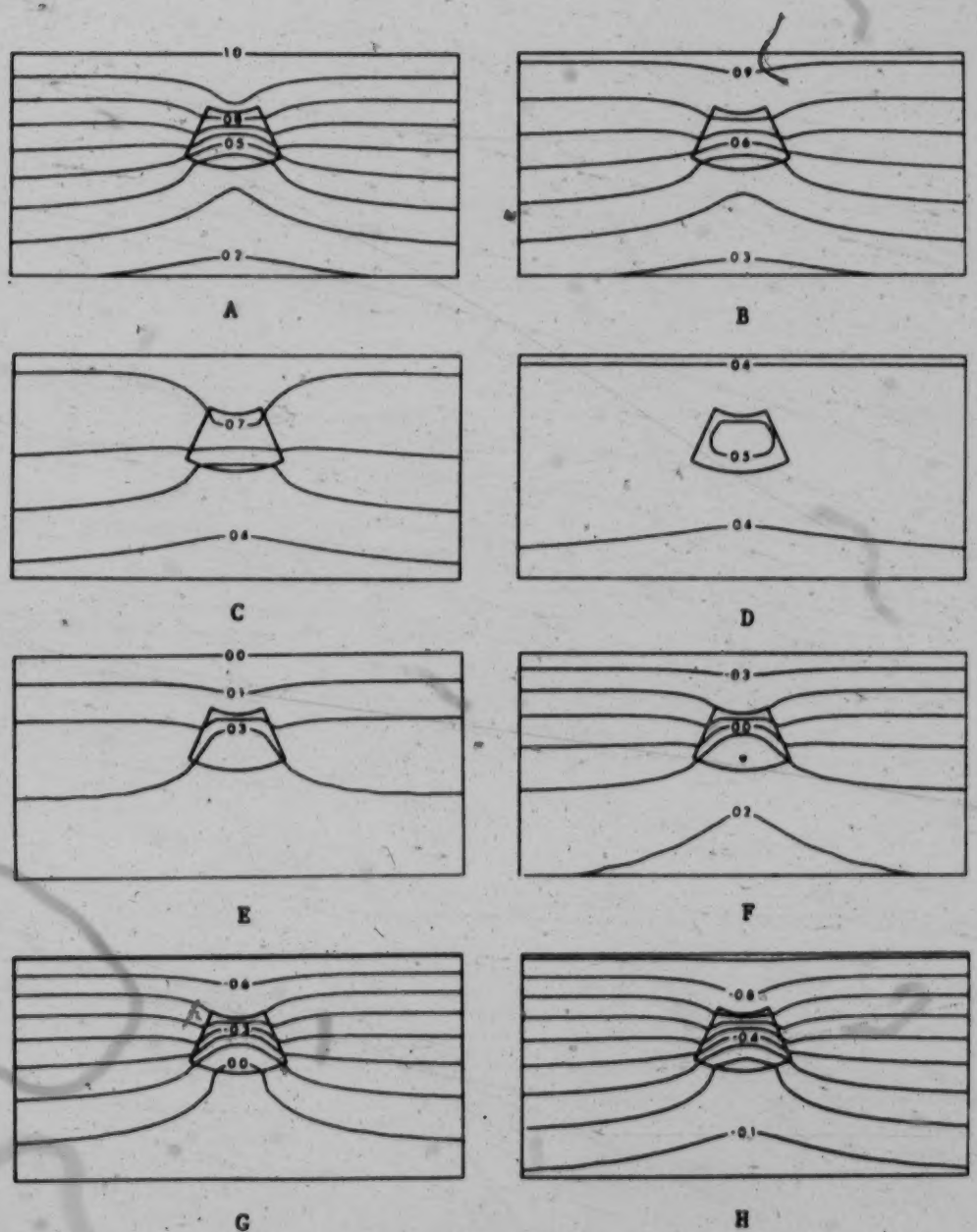

Figure 21 Dyke model, H-polarization. Contours of equal H_z at equal intervals of one-sixteenth of the period. (T = 10 sec)

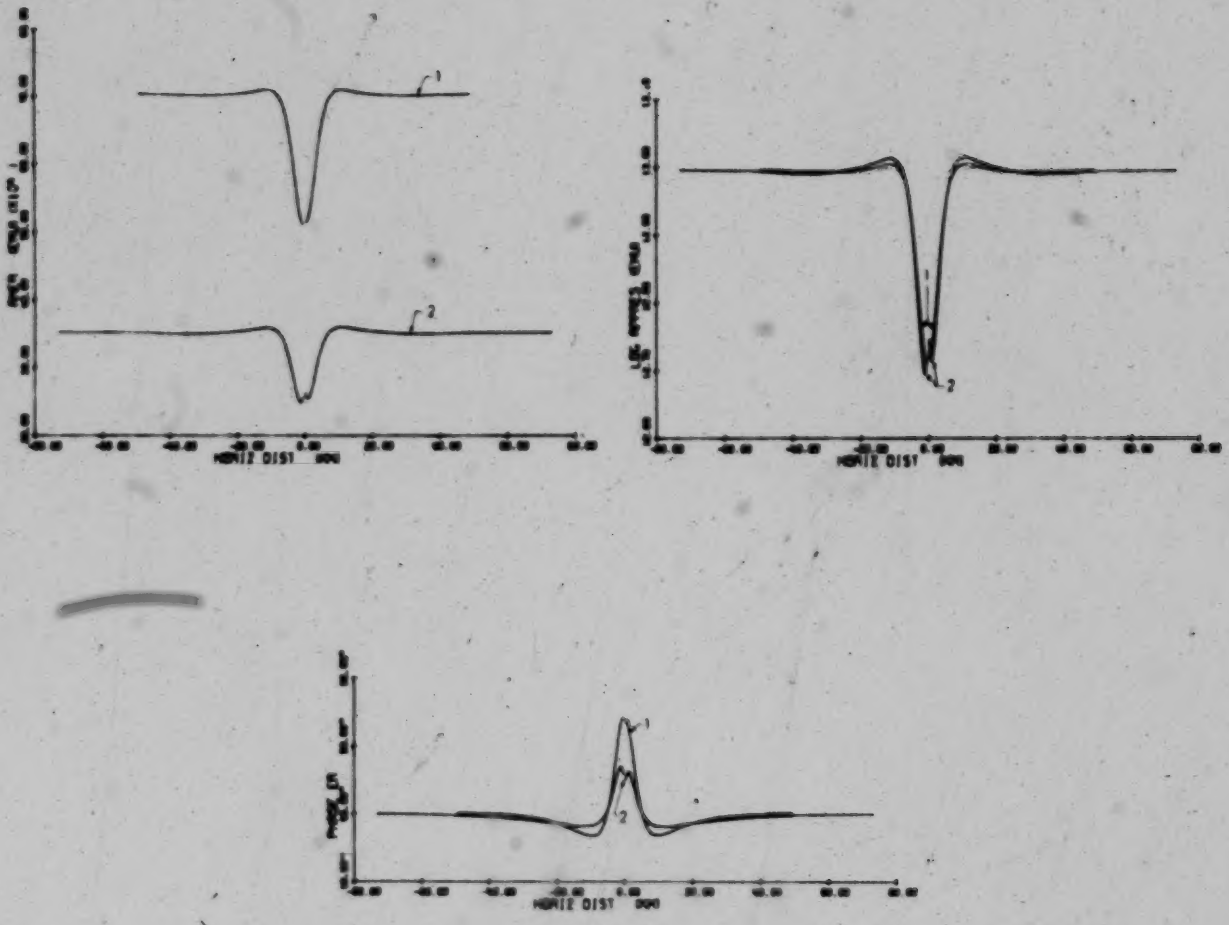

Figure 22 Dyke model, H-polarization. Amplitude and phase profiles of E_x and ρ_x.
Curves 1: T = 10 sec; curves 2: T = 40 sec.

width of the top of the structure. Since the vertical size of the dyke exceeds the skin depth for the shorter period, the currents penetrate only slightly into the region of higher resistivity below the structure.

4.3.3 E-polarization

Figure 20 exhibits the amplitude contours of E_z for both periods investigated. For the shorter period the current density is higher above and inside the buried dyke than at a corresponding depth in the surrounding poor conductor farther away from the structure. For the longer period the contours do not deviate greatly from a uniform configuration. Since the conductivity is 25 times higher inside the structure than in the surrounding material, it is apparent that the current density increases inside the dyke.

The contours of equal E_z at different epochs of the 10 sec oscillation period are shown in Figure 23. The currents flowing parallel to the strike of the dyke are concentrated inside the structure during the whole cycle. The contours, which correspond to the lines of force of the magnetic field, are strongly curved near the structure. At the beginning of the first and second quarter of the oscillation period current wedges are observed around the better conducting region.

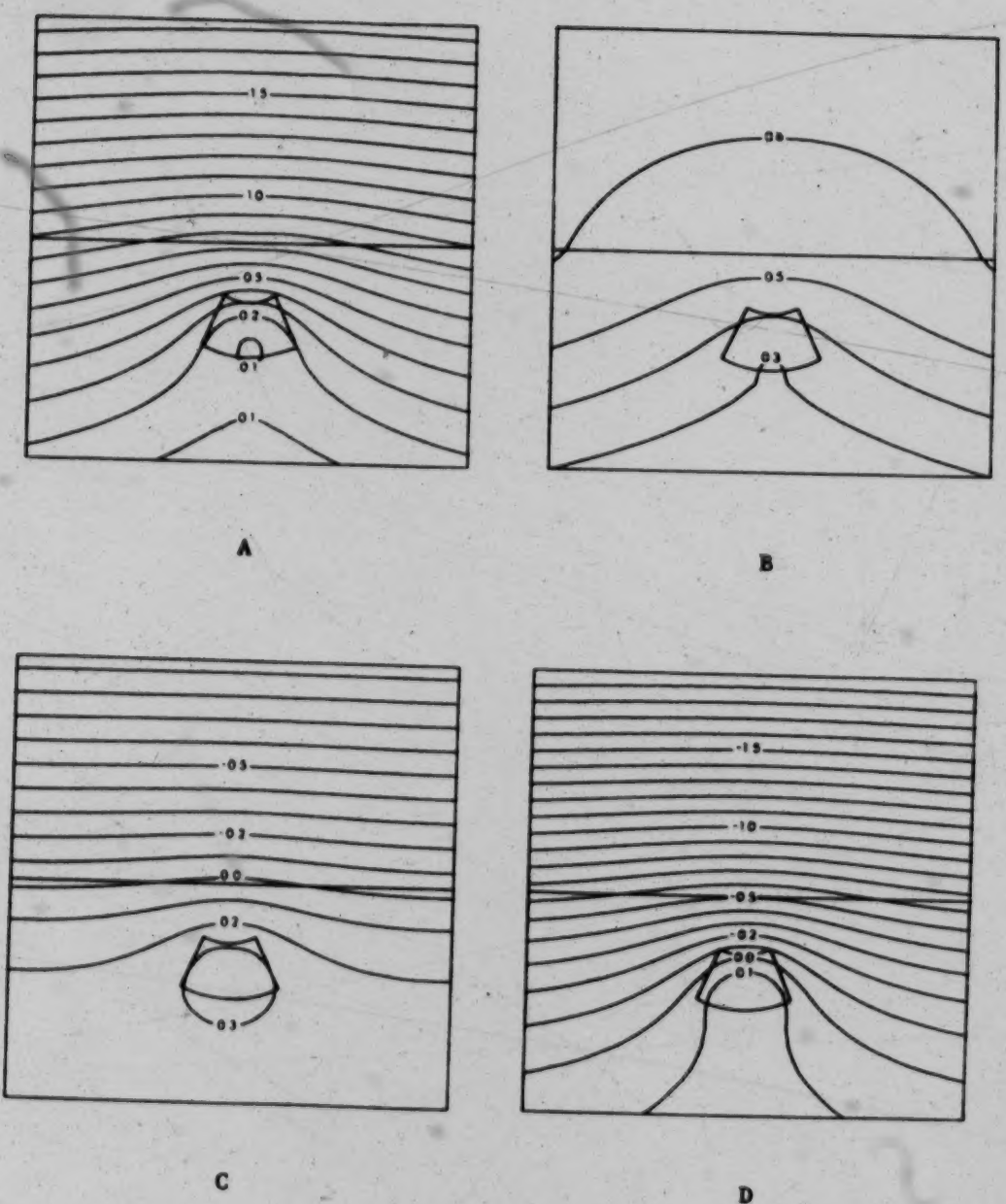

A B C D

Figure 23 Dyke model, E-polarization. Contours of equal E_z at equal intervals of one-eighth of the period.

Figures 24 and 25 illustrate the surface values of the field components. Less asymmetry than in the H-polarization is observed in the H_r and correspondingly in the ρ_z values. The apparent resistivity values differ from each other for the two periods and this difference is much greater than in the H-polarization case. The surface values outside a distance of about 40-50 km from the center of the structure nearly correspond to those of a uniform field for the 40 sec period. This distance is less for the 10 sec period. The resistivity above the dyke is greater for the longer period than for the shorter since the currents penetrate into the higher resistivity region under the structure. The change in the phase values of H_r and ρ_z is opposite for the two different periods. Also H_r shows a greater and wider maximum for the longer period. E_z values decrease above the structure. The minimum value is less for the shorter period since the thickness of the dyke exceeds the skin depth in the better conductor. For the 40 sec period there is a small local maximum in the E_z values above the top of the structure. This shows the effect of the thicker lower conductivity region above the center of the dyke. There is a characteristic pair of maxima in the H_ϕ values. The distance between them is greater than the width of the structure. The maximum value, which occurs approximately at the same position for both

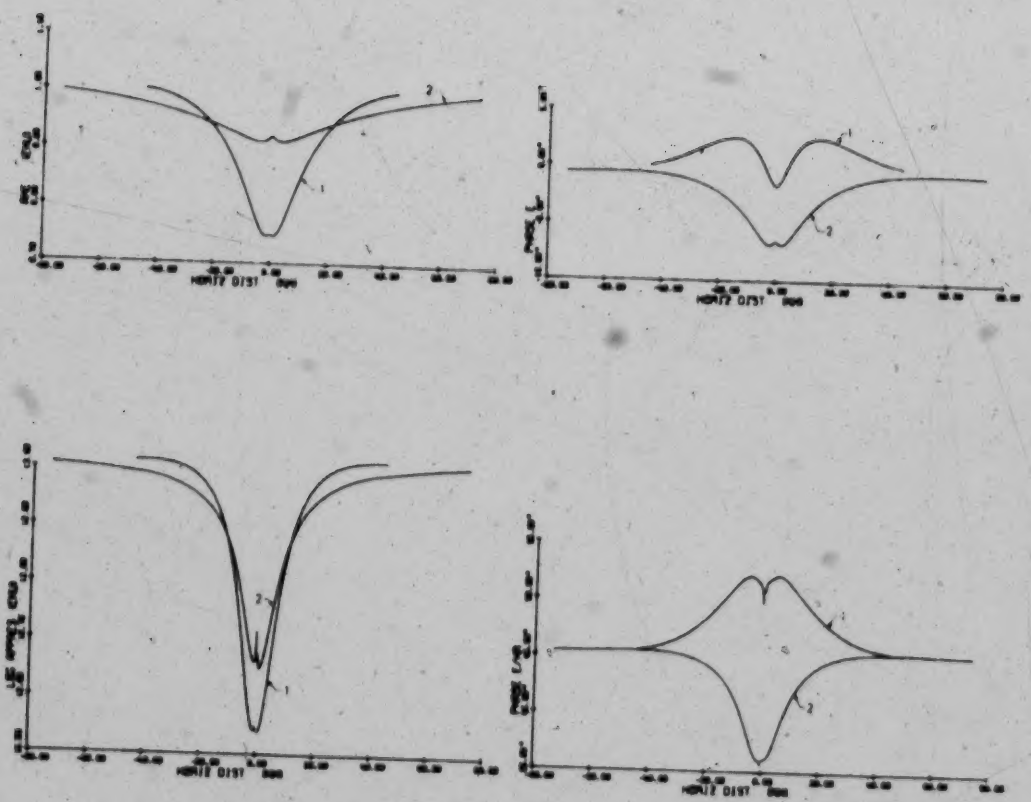

Figure 24 Dyke model, E-polarization. Amplitude and phase profiles of E_z add ρ_a. Curves 1: T = 10 sec; curves 2: T = 40 sec.

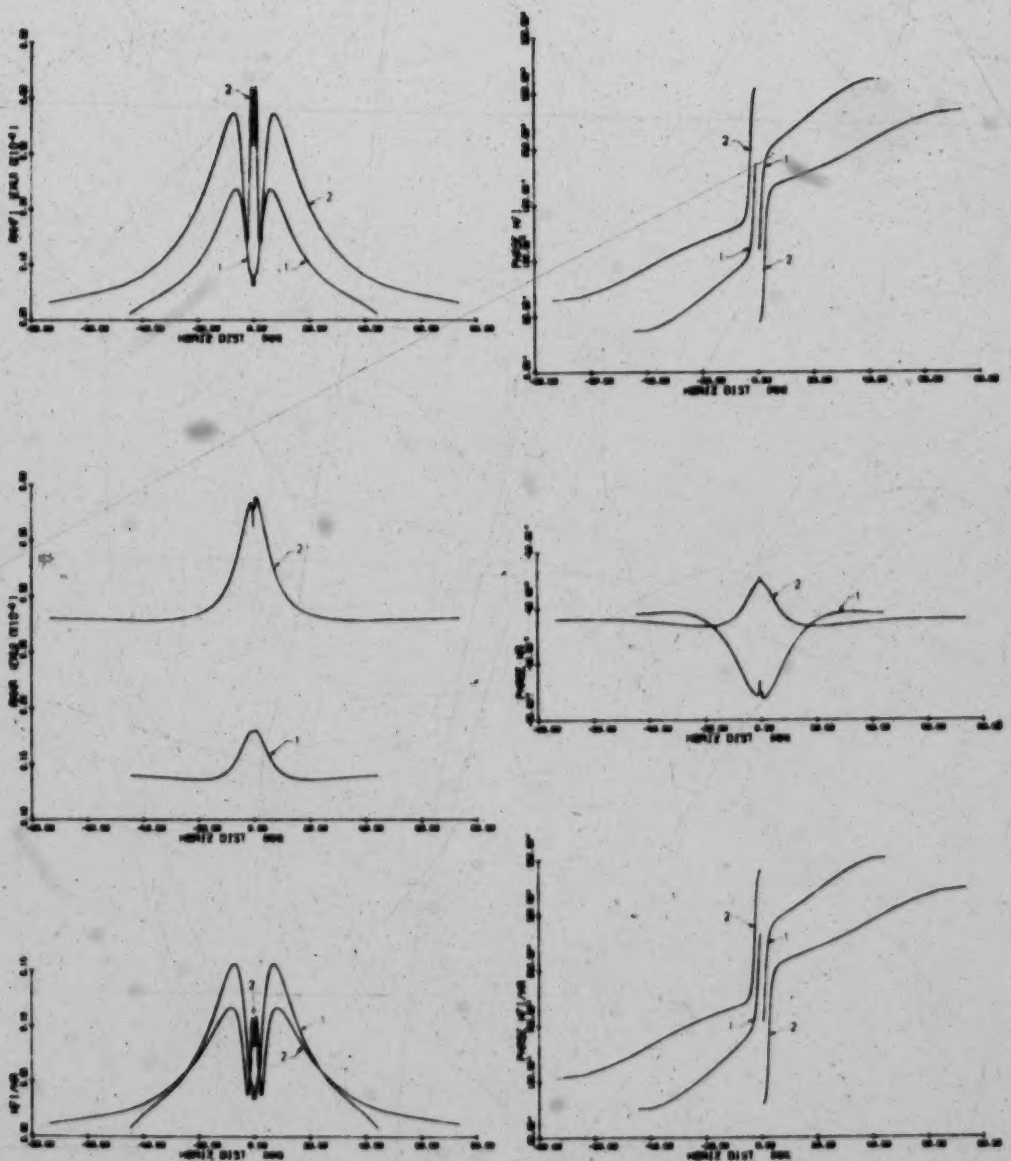

Figure 25 Dyke model, E-polarization. Amplitude and phase profiles of H_ϕ, H_r and H_ϕ/H_r. Curves 1: T = 10 sec, curves 2: T = 40 sec.

periods, is greater for the longer period. These maxima are observed in the H_ϕ/H_r values as well, but the maximum value for the shorter period becomes larger than that of the longer period. Another pair of maxima in the H_ϕ values, which is present just above the dyke and only for the longer period, is much less dominant in the profile of the ratio of the two components. As with the ridge model, the vertical magnetic component is zero above the central point and changes sign there.

4.4 The Sloping Contact Model

4.4.1 General

The five different sloping contacts studied in the present work are shown in Figure 10. The resistivity of the material is 10Ωm above the sloping discontinuity and 100Ωm throughout the remainder of the conducting region. The oscillation period of the alternating source field is 40 sec in each case. This period gives a skin depth of 10.0 km for the better conductor and 31.8 km for the high resistivity material. The two different sets of grid spacings used in the radial direction are presented in Table 3. The maximum radius of the mesh is 103.5 km in set A and 103.2 km in set B. The four sets of angular grid spacings which are applied for the different slopes are given in Table 4. The calculations are done in MKS units.

Table 3

The Radial Grid Spacings for the Sloping Contacts

(Δr values are in kms from the central point toward the external boundary)

Set A: .8, .1, .12, .14, .17, .2, .24, .29, .34, .4, .47, .58, .7, .84, 1., 1.2, 1.45, 1.75, 2.1, 2.4, 2.8, 3.3, 3.9, 4.6, 5.3, 6.2, 7.1, 8., 8.5, 9., 9.5, 10., 10.

Set B: .4, .1, .11, .12, .14, .17, .2, .24, .29, .34, .4, .47, .58, .7, .84, 1., 1.2, 1.45, 1.75, 2.1, 2.4, 2.8, 3.3, 3.9, 4.6, 5.3, 6.2, 7.1, 8., 8.5, 9., 9.5, 10., 10.

Table 4

The Angular Grid Spacings for the Sloping Contacts

($\Delta\phi$ values are in degrees in a clockwise direction beginning at the surface on the right-hand side of the model)

Set a: 1.5, 2, 2.2, 3, 4, 5.3, 6, 6, 6, 6, 6, 7, 7, 7, 7, 7,
7, 7, 7, 7, 7, 6, 6, 6, 6, 6, 5.3, 4, 3, 2.2, 2, 1.5,
1.5, 2, 3, 4, 5, 5.5, 6, 7, 8, 8, 8, 8, 8, 8, 8,
8, 8, 8, 8, 8, 8, 8, 7, 6, 5.5, 5, 4, 3, 2, 1.5

Set b: 2.5, 3.2, 4, 5, 5.3, 6, 6, 6, 6, 6, 6, 6, 6, 6, 6, 5, 5,
5, 5, 6, 6, 6, 6, 6, 6, 6, 6, 6, 6, 5.3, 5, 4, 3.2, 2.5,
2.5, 3.2, 4, 5, 5.3, 7, 7, 7, 7, 7, 7, 7, 7, 7, 7,
7, 7, 7, 7, 7, 7, 7, 7, 7, 7, 5.3, 5, 4, 3.2, 2.5

Set c: 3, 4, 4.7, 5.5, 6, 6, 5.8, 5, 5, 5, 6, 6, 6, 6, 6, 5, 5,
5, 5, 6, 6, 6, 6, 6, 5, 5, 5, 5.8, 6, 6, 5.5, 4.7, 4, 3,
3, 4, 4.7, 5.5, 6, 6, 6, 6, 7, 7, 7, 7, 7, 7, 6.8,
6.8, 7, 7, 7, 7, 7, 7, 6, 6, 6, 6, 5.5, 4.7, 4, 3

Set d: 3, 4, 4.7, 5, 5, 5, 5.5, 5.8, 6, 6, 6, 6, 6, 6, 6, 5, 5,
5, 5, 6, 6, 6, 6, 6, 6, 6, 5.8, 5.5, 5, 5, 5, 4.7, 4, 3,
3, 4, 4.7, 5, 5, 5, 5.5, 6.8, 7, 7, 7, 7, 7, 8, 8,
8, 8, 7, 7, 7, 7, 7, 6.8, 5.5, 5, 5, 5, 4.7, 4, 3

4.4.2 H-polarization

In the H-polarization case only four of the sloping models are studied. The following sets of grid spacings are used for the different slopes:

B-b for $\alpha_1 = 5.7^\circ$

B-c for $\alpha_2 = 11.7^\circ$

B-c for $\alpha_4 = 45^\circ$

B-c for $\alpha_5 = 90^\circ$

Figure 26 shows the amplitude contours of H_z for each slope. It is well illustrated that the electric currents tend to flow in the region of higher conductivity. In the vertical contact case the current flow depends on the different skin depths in the two regions. The current lines are strongly refracted at the boundary between the different conductivity regions. This refraction of the current lines is caused by slowly varying surface charges at the interface as discussed by Jones and Price (1971a, 1971c) and Price (1973). It is the surface charges built up at any interface inside the conductor which spread the current lines at the discontinuities in the other two models as well. Since there is more than one discontinuity in the ridge and dyke models, the picture is more complicated. In general current lines are refracted at all interfaces near lateral inhomogeneities.

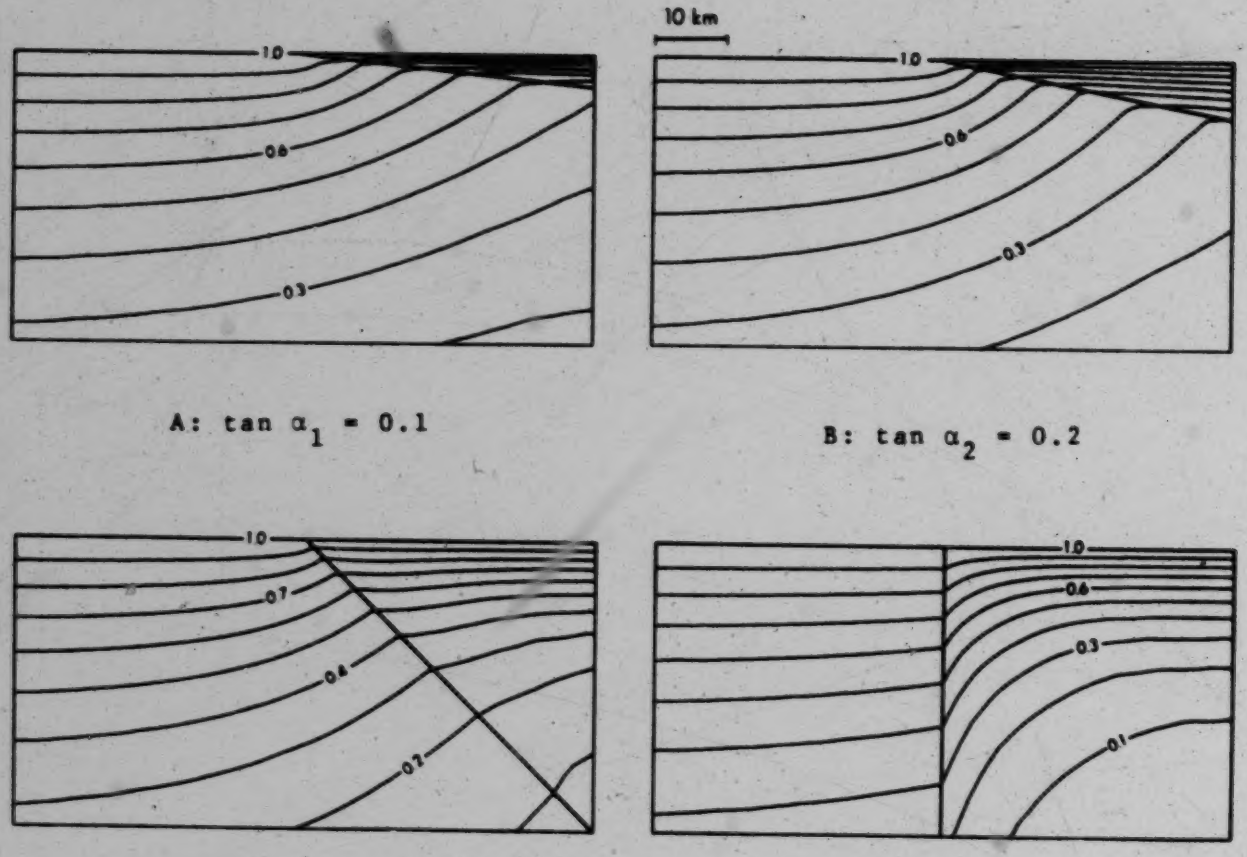

A: tan α_1 = 0.1

B: tan α_2 = 0.2

C: tan α_4 = 1.0

D: tan α_5 = ∞

Figure 26 Sloping contact models, H-polarization. Amplitude contours of H_z. (T = 40 sec)

The field configuration at different epochs of the oscillation period for the 45° slope are exhibited in Figure 27. At the beginning of the period the distortion of the current lines, which are parallel to the surface at great distances from the discontinuity, increases with depth near the discontinuity, especially in the better conductor. After a quarter period current loops are formed near the surface in the higher conductivity region. During the second quarter of the period these current vortices move downward and decay. For the smaller slopes the current lines are less curved than in the case discussed above. For the vertical contact there is an even stronger tendency to form current vortices in the better conductor during the oscillation.

The amplitudes of the surface values in Figure 28 show a discontinuity at the central point. Near the interface on the higher resistivity side E_r and ρ_r are much greater than their asymptotic values. Apart from the vertical contact, which shows a slight increase only, the values near the interface increase with increasing α and the maximum value appears for $\alpha_4 = 45^\circ$. The surface values correspond to those of a uniform field outside a distance of about 30-40 km from the center depending on the slope of the discontinuity on the other side. On the higher conductivity side the amplitudes of E_r and ρ_r for the smaller slopes gradually decrease with

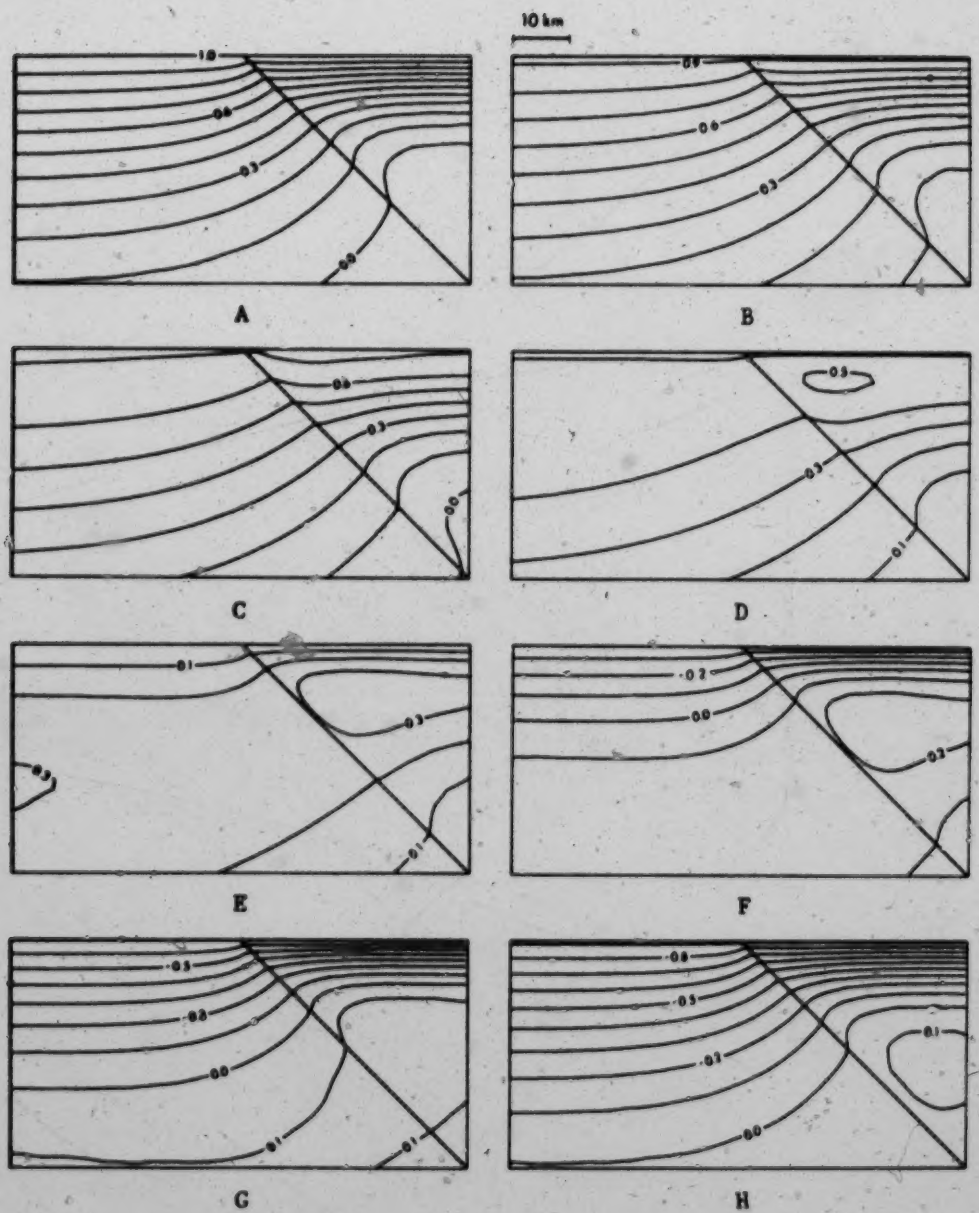

Figure 27 The sloping contact model with tan α_4 = 1.0, H-polarization. Contours of equal H_z at equal intervals of one-sixteenth of the period.

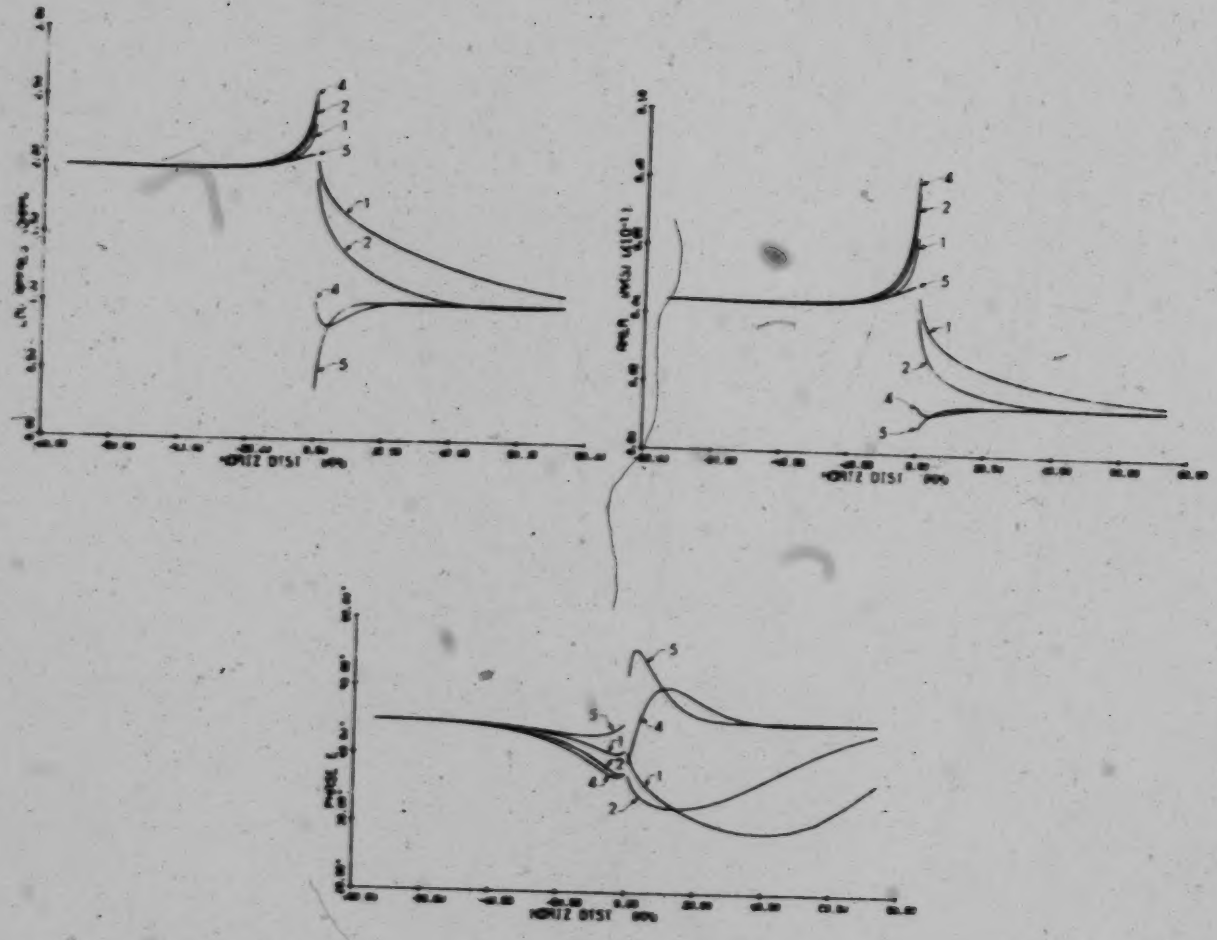

Figure 28 Sloping contact models, H-polarization.
Amplitude and phase profiles of E_r and ρ_r.
Curves 1: tan α_1 = 0.1; curves 2: tan α_2 = 0.2;
curves 4: tan α_4 = 1.0; curves 5: tan α_5 = ∞
(T = 40 sec).

distance from the center where the discontinuity intersects the surface. Also, these values approach their asymptotic values at a distance where the discontinuity is at a depth approximately equal to the skin depth there. The phase profile reaches 45°, which corresponds to a uniform field configuration, farther away from the center. For the 45° slope the amplitudes near the discontinuity are smaller than the asymptotic values and show a minimum at a distance of about 4 km from the central point. The curves correspond to those of a uniform field outside a distance of about 25 km for the amplitudes and 35 km for the phases. In the vertical contact case the amplitude drops to a very small value and the asymptotic value is reached at a distance of about 15 km while the asymptotic value in the phase is reached at about 25 km from the interface.

4.4.3 E-polarization

In the E-polarization case different combinations of the sets of radial and angular grid spacings are used so that the effect of changing the mesh may be studied. The applied pairs of sets are:

A-b	and	B-a	for	$\alpha_1 = 5.7^\circ$
A-c	and	B-c	for	$\alpha_2 = 11.7^\circ$
		B-d	for	$\alpha_3 = 26.7^\circ$
A-c			for	$\alpha_4 = 45^\circ$
A-c	and	B-c	for	$\alpha_5 = 90^\circ$

Figure 29 shows the amplitude contours for the electric field for the slopes that have been discussed in the H-polarization case as well. The change in the field configuration depending on α shows the effect of the region of higher conductivity. The currents flowing parallel to the strike of the slope are highly concentrated near the surface in the better conducting region.

The contours of equal E_z at different epochs for one-half of the cycle are exhibited in Figure 30 for the 45° slope. At the beginning of this half of the cycle the direction of the magnetic field presented by the contours is almost horizontal except near the discontinuity. After one-eighth of the period the direction of the field changes and is mainly vertical. Also, in this time interval the field magnitude has decreased. During the second quarter of the period the magnetic lines of force form loops in the better conductor. This shows that the corresponding positive currents are concentrated there. There are increasing negative currents near the surface.

The surface values calculated using set A for the radial grid spacings are presented in Figures 31 and 32 while Figures 33 and 34 show the surface values determined applying set B. There is some difference between the corresponding profiles in the two sets of figures for the two small slopes

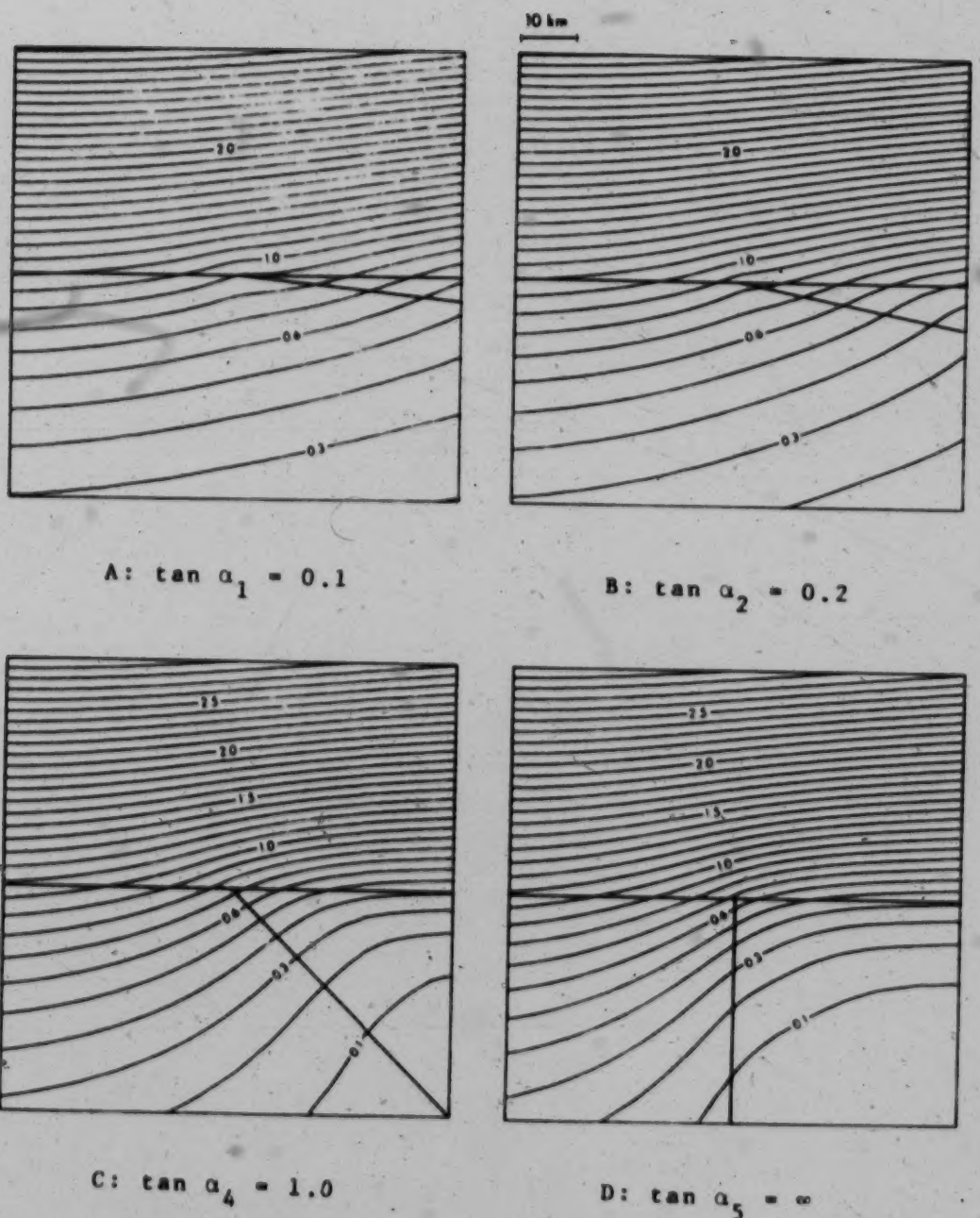

A: tan α_1 = 0.1

B: tan α_2 = 0.2

C: tan α_4 = 1.0

D: tan α_5 = ∞

Figure 29 Sloping contact models, E-polarization. Amplitude contours of E_z. (T = 40 sec)

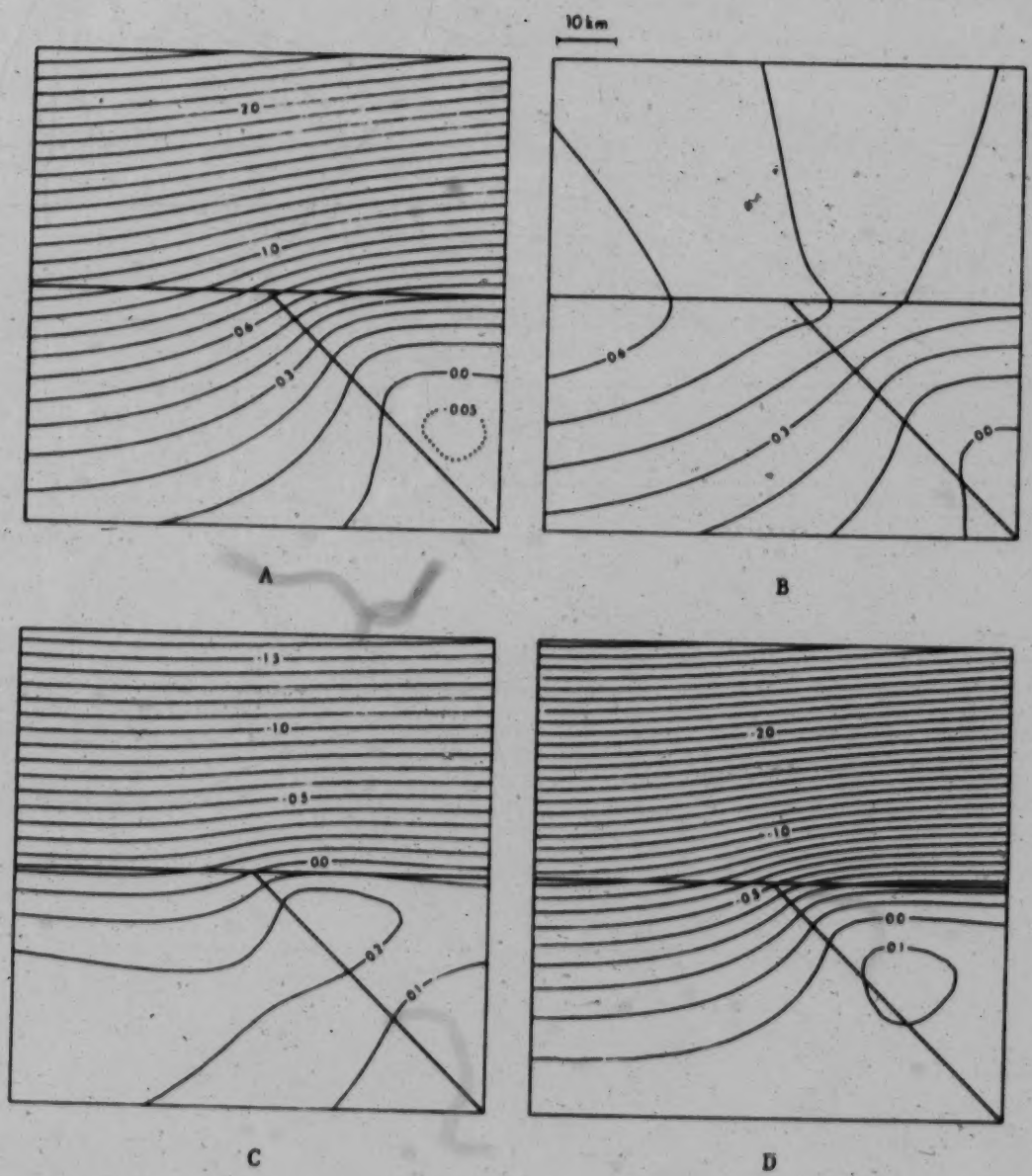

Figure 30 The aloping contact model with tan α_4 = 1.0, E-polarization. Contours of equal E_z^4 at equal intervals of one-eighth of the period. (T = 40 sec)

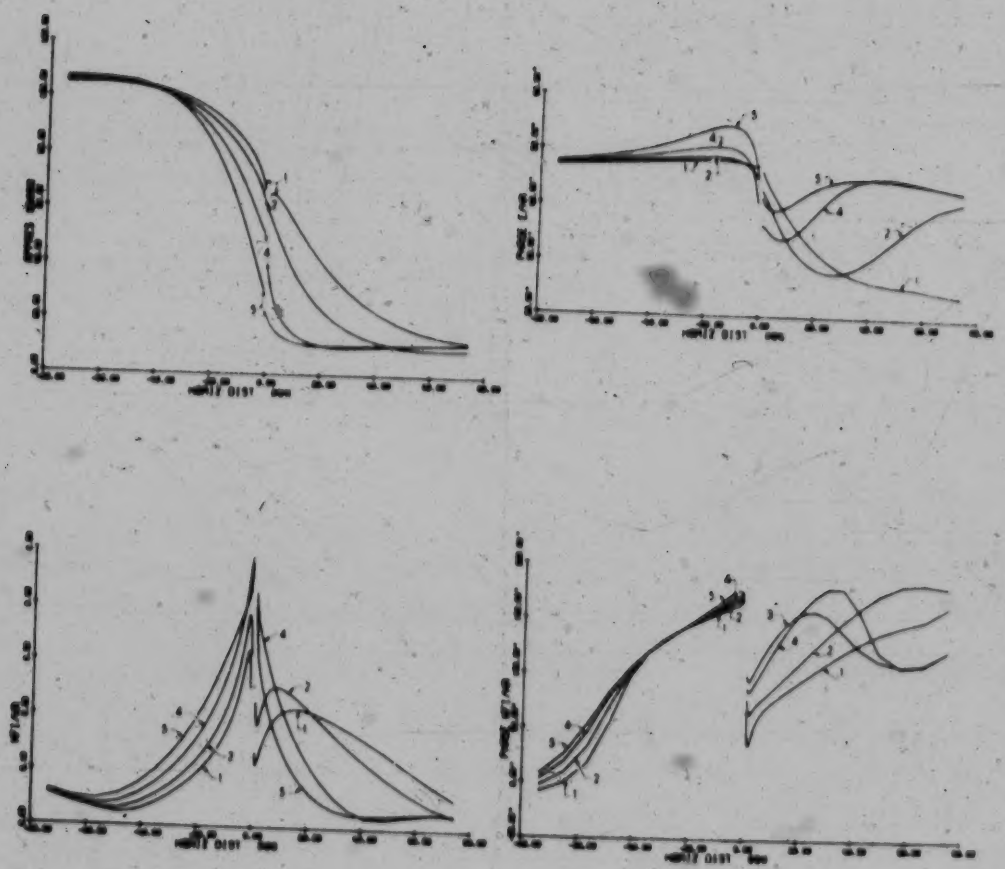

Figure 31 Sloping contact models, E-polarization. Amplitude and phase profiles of ρ_- and H_ϕ/H_r using set A in Table 3 for the radial grid spacings of the mesh.
Curves 1: $\tan\alpha_1 = 0.1$; curves 2: $\tan\alpha_2 = 0.2$; curves 4: $\tan\alpha_4 = 1.0$; curves 5: $\tan\alpha_5 = \infty$
(T = 40 sec)

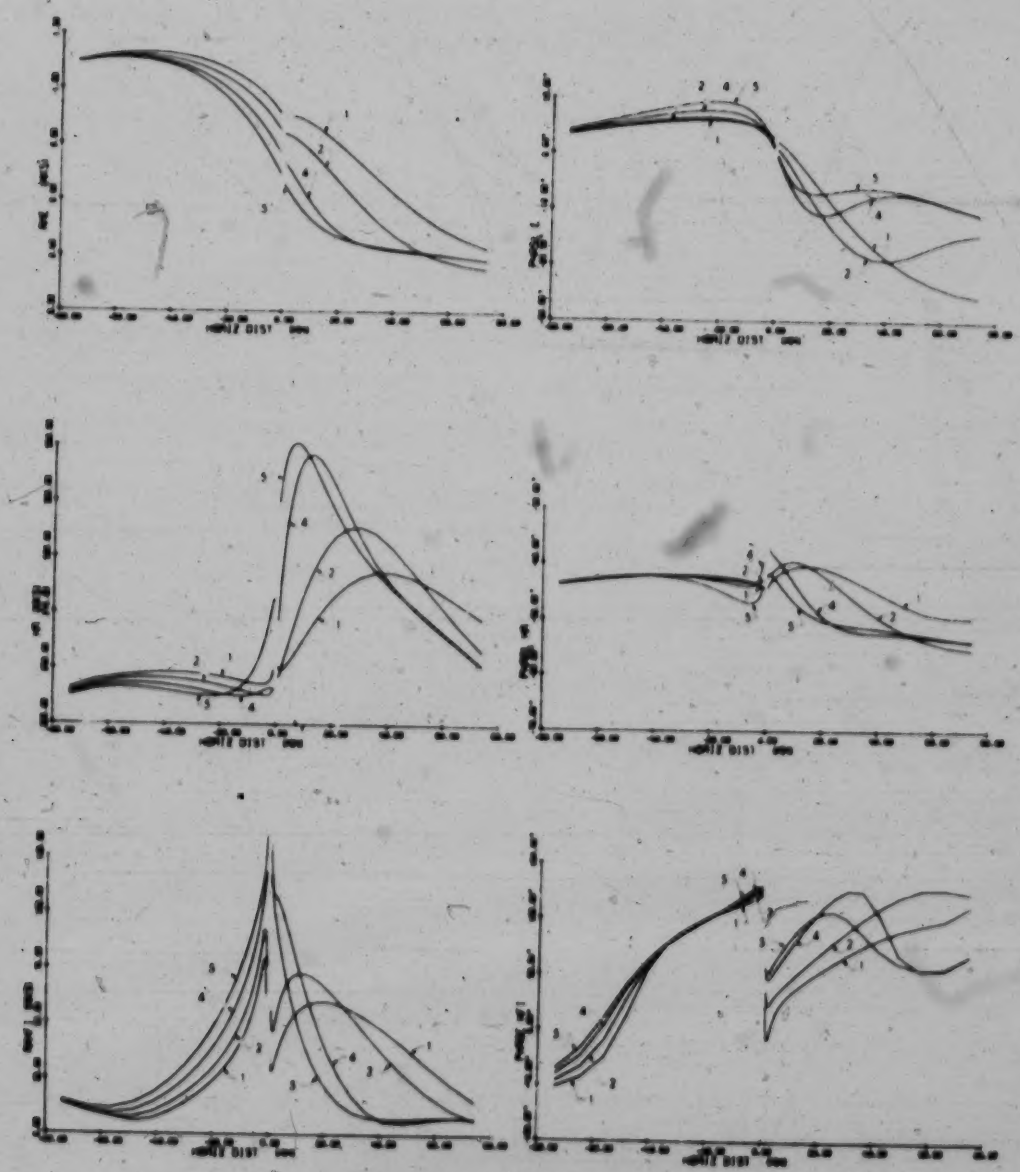

Figure 32 Sloping contact models, E-polarisation. Amplitude and phase profiles of E_z, H_r and H_ϕ using set A in the grid. Curves 1: $\tan \alpha_1 = 0.1$; curves 2: $\tan \alpha_2 = 0.2$; curves 4: $\tan \alpha_4 = 1.0$; curves 5: $\tan \alpha_5 = \infty$ (T = 40 sec)

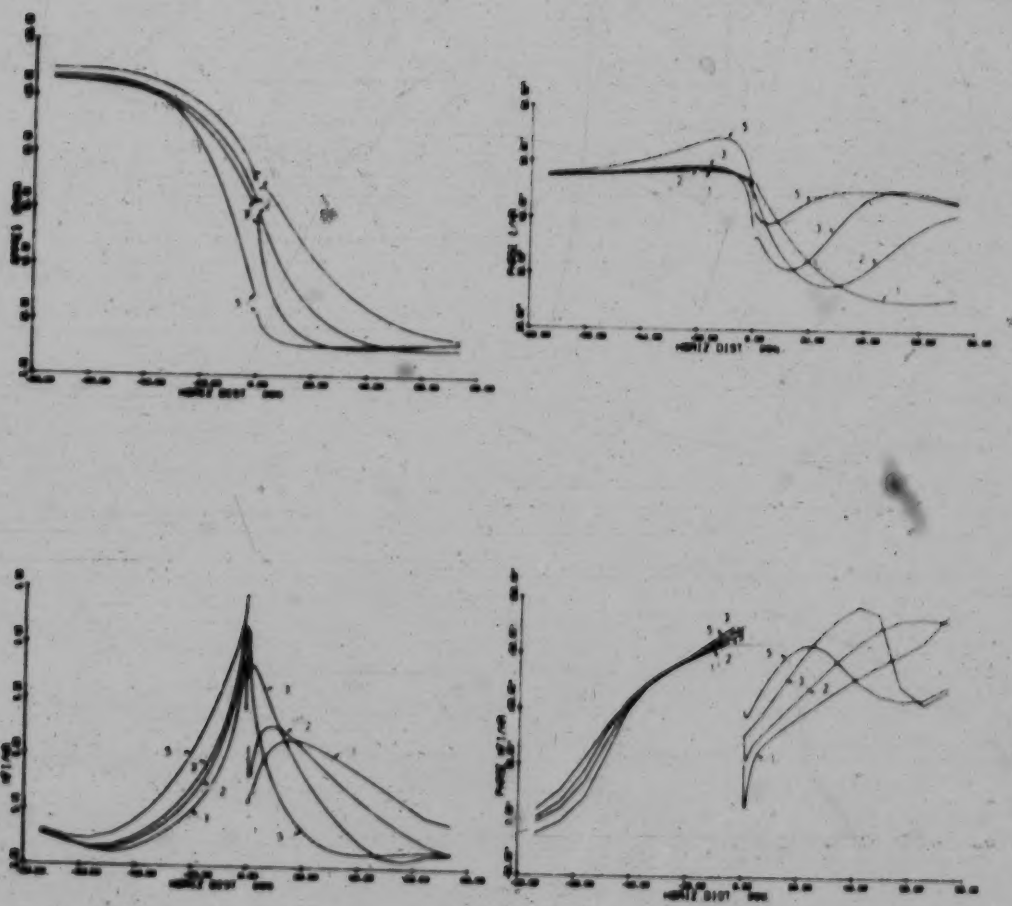

Figure 33 Sloping contact models, E-polarization. Amplitude and phase profiles of ρ_s and H_ϕ/H_r using set B in Table 3 for the radial grid spacings of the mesh.
Curves 1: tan α_1 = 0.1; curves 2: tan α_2 = 0.2; curves 3: tan α_3 = 0.5; curves 5: tan α_5 = ∞
(T = 40 sec)

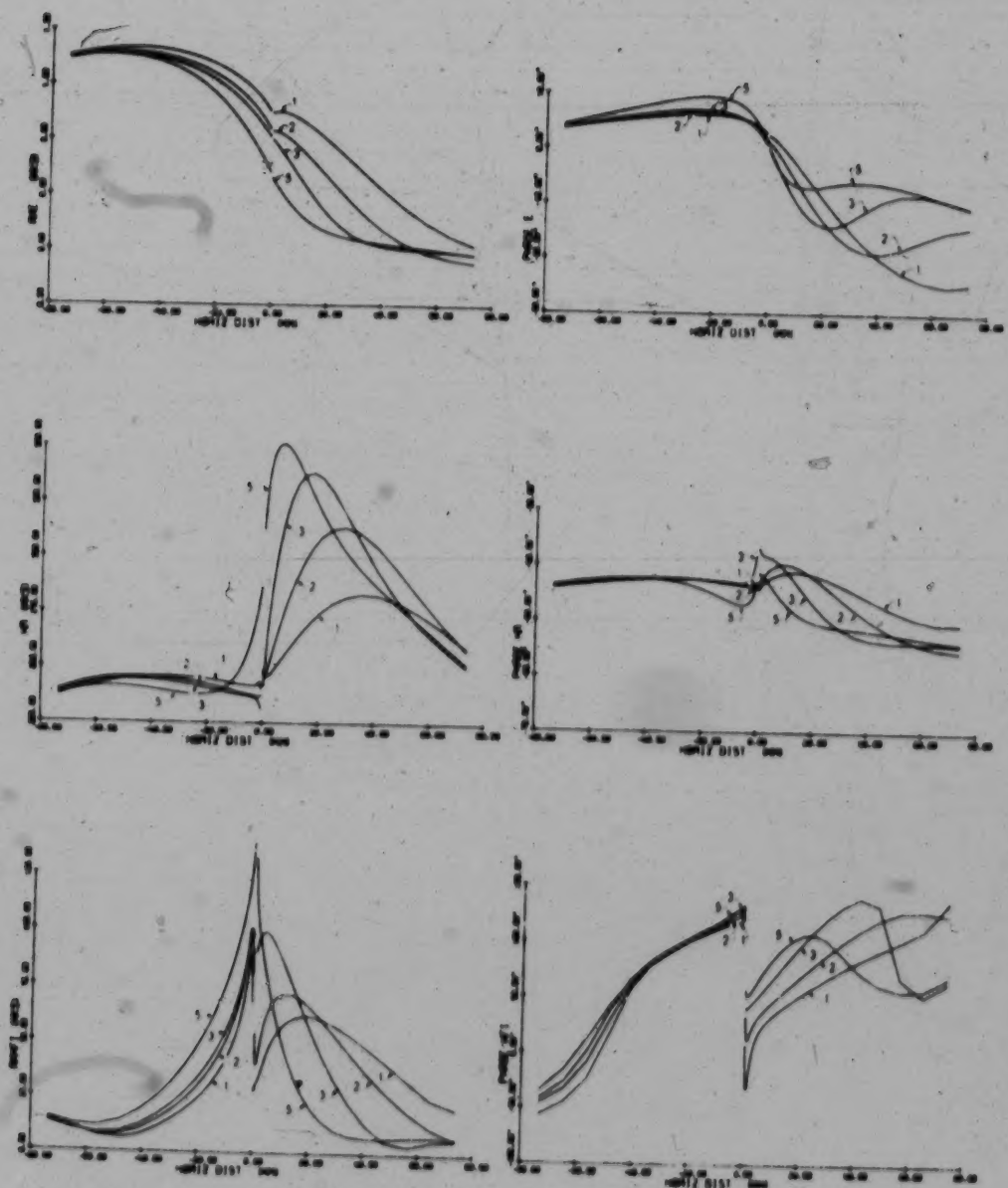

Figure 34 Sloping contact models, E-polarization. Amplitude and phase profiles of E_z, H_r and H_ϕ using set B in the grid. Curves 1: $\tan \alpha_1 = 0.1$; curves 2: $\tan \alpha_2 = 0.2$; curves 3: $\tan \alpha_3 = 0.5$; curves 5: $\tan \alpha_5 = \infty$ (T = 40 sec)

near the central point. The calculated surface values depend on the size of the mesh to a certain extent, particularly if the maximum arc of the grid is not large enough and there is a considerable deviation from the uniform field near the surface at the extremities of the model as discussed in section 3.2. In the case of the smallest slope the depth to the discontinuity is slightly greater than the skin depth for the better conductor at the external boundary of the mesh and the boundary conditions are not satisfied perfectly. Also, the iteration cannot be done in an optimum manner inside and adjacent to the better conductor. The values of B_1, B_2, B_3 and B_4 in equations (2.8a and b) are not of the same order of magnitude since the distances from point '0' to points '2' and '4' are much greater than the distances to points '1' and '3' (see Figure 2).

Differences in the electric field values are negligible except for the greater dips in the middle of the curves as calculations are made nearer the central point. Differences are evident in the horizontal magnetic field values and correspondingly in the apparent resistivity values in the central region. The vertical contact profiles are equivalent in the two figures.

The H_r and H_ϕ amplitude curves both show maxima on the better conductivity side. These maxima are shifted to-

ward the higher resistivity region as α increases. The maxima in the horizontal magnetic field values appear farther away from the center than they do in the vertical component. As a result there are maxima in the H_ϕ/H_r values which are narrower and shifted toward the center when compared with the curves of H_r and H_ϕ. The maximum for the 26.7° slope lies between the maxima of the profiles for the 11.7° and 45° slope for both magnetic components and correspondingly for the ratio as well. The H_ϕ component has another even greater maximum on the higher resistivity side. This is quite near the point where the discontinuity intersects the surface. It shifts slightly toward the better conductor as α increases. In the vertical contact case the two maxima coincide at the central point. Since the horizontal component of the magnetic field does not show considerable changes above the lower conductivity region, the maximum of the vertical component dominates in the ratio H_ϕ/H_r .

The apparent resistivity values show a gradual change between the two asymptotic values. The lower resistivity value is more slowly approached in the case of the smaller slopes since the depth of the higher conductivity material is less than the skin depth even at large distances from the central point.

According to the surface values, in particular the ρ_z and H_ϕ/H_r curves since H_r does not change much, the field configuration can be considered as uniform outside a distance of about 40-50 km from the center on the high resistivity side. This distance is larger for the vertical contact than for the small slopes. In the H-polarization case this distance is the smallest for the 90° slope. Above the slope the uniform field configuration appears at a distance of about 30 km for the vertical contact. The amplitude of the apparent resistivity reaches its asymptotic value at an even smaller distance. This distance increases with decreasing α and for the smallest slope it exceeds the radius of the outermost arc of the mesh. The discontinuity affects the field configuration near the surface at the external boundary as discussed above.

CHAPTER 5 CONCLUSIONS

The perturbations of a uniform alternating electromagnetic field by three different two-dimensional conductivity inhomogeneities has been studied in this thesis. The calculations have been made using a cylindrical co-ordinate system which is more appropriate than the Cartesian co-ordinate system for the models considered. The field configurations near the non-uniform region of the conductive area have been given as well as the change of each field component along the surface.

Several sloping contacts were examined by other authors using different methods. The present study applies a more acceptable boundary condition than that of Geyer (1972). Also, the present work gives a better approximation to the geometry of the slope than that used by Jones and Price (1971a). Furthermore, more details about the surface values are given than those in the paper by Reddy and Rankin (1973). Also, greater slopes than Blake (1970) used are examined.

Some horizontal inhomogeneities were investigated by Jones and Price (1971b) changing the depth and vertical size of the structure. However, there was only one oscillation period studied. Also, Rankin (1962) examined the electromagnetic effect on a dike just below the surface in the H-polarization case only.

Some limitations of the finite difference method, particularly considering the choice of mesh (see section 3.2) may be examined in more detail in future. The asymmetry effect of the iteration procedure (see section 3.4) must be further investigated as well. Also, better approximations for the first derivatives of the field values in equations (2.6a and b) should be considered. The approximation used here assumes a linear change of the first derivatives which is inaccurate near the inhomogeneities even if the adjacent grid spacings do not differ from each other. At the extremities of the grid near the surface the field values change more in the relatively large angular grid spacings than is given by the linear approximation because the electromagnetic field decreases exponentially with depth inside a uniform conductor.

The substitution of finite differences may cause a slight change in the field values in the E-polarization case just inside the external boundaries along the surface where the uniform field configuration is not distorted by the inhomogeneities. This effect is particularly observed in Figure 17 where far from the ridge the surface values of the electric field are less than 1 which is the normalized F_z value at the external boundary. For the sloping contact the electric field increases over the normalized surface value on the high resistivity side as illustrated in Figures 32 and 34.

REFERENCES

Blake, J. R., 1970. The effect of a sloping sea floor on the surface electromagnetic field. J. Geomagn. Geoelect. 22, 421-440.

Cagniard, L., 1953. Basic theory of the magneto-telluric method of geophysical prospecting. Geophysics 18, 605-635.

Coggon, J. H., 1971. Electromagnetic and electrical modeling by the finite element method. Geophysics 36, 132-155.

Dosso, H. W., 1966. Analogue measurements for electromagnetic variations near the coastline. Can. J. Earth Sci. 3, 917-936.

d'Erceville, I. and Kunetz, G., 1962. The effect of a fault on the Earth's natural electromagnetic field. Geophysics 27, 651-665.

Geyer, R. G., 1972. The effect of a dipping contact on the behaviour of the electromagnetic field. Geophysics 37, 337-350.

Jones, F. W. and Pascoe, L. J., 1971. A general computer program to determine the perturbation of alternating electric currents in a two-dimensional model of a region of uniform conductivity with an embedded inhomogeneity. Geophys. J. R. Astr. Soc. 23, 3-30.

Jones, F. W. and Price, A. T., 1970. The perturbations of alternating geomagnetic fields by conductivity anomalies. Geophys. J. R. Astr. Soc. 20, 317-334.

Jones, F. W. and Price, A. T., 1971a. Geomagnetic effects of sloping and shelving discontinuities of earth conductivity. Geophysics 36, 58-66.

Jones, F. W. and Price, A. T., 1971b. The geomagnetic effects of two-dimensional conductivity inhomogeneities at different depths. Geophys. J. R. Astr. Soc. 22, 333-345.

Jones, F. W. and Price, A. T., 1971c. Reply by authors to discussion by John F. Hermance. Geophysics 37, 541-542.

Lahiri, B. N. and Price, A. T., 1939. Electromagnetic induction in non-uniform conductors, and the determination of the conductivity of the earth from terrestrial magnetic variations. Phil. Trans. Roy. Soc. London 237, A, 509-540.

Madden, T. and Thompson, W., 1965. Low frequency electromagnetic oscillations of the earth-ionosphere cavity. Revs. of Geophys. 3, 211-254.

Neves, A. S., 1957. The generalized magneto-telluric method, Ph.D. Thesis, Dept. of Geol. and Geophys., M.I.T.

Pascoe, L. J. and Jones, F. W., 1972. Boundary conditions and calculation of surface values for the general two-dimensional electromagnetic induction problem. Geophys. J. R. Astr. Soc. 27, 179-193.

Patrick, F. W. and Bostick, F. X., 1969. Magnetotelluric modeling techniques. Techn. Rept. 59, Electronic Research Center, Univ. of Texas, Austin.

Price, A. T., 1950. Electromagnetic induction in a semi-infinite conductor with a plane boundary. Quart. J. Mech. and Applied Math. 3, 385-410.

Price, A. T., 1964. A note on the interpretation of magnetic variations and magnetotelluric data. J. Geomagn. Geoelect. 15, 241-248.

Price, A. T., 1973. The theory of geomagnetic induction. Physics of the Earth and Planetary Interiors 7, 227-233.

Rankin, D., 1962. The magnetotelluric effect on a dike. Geophysics 27, 666-676.

Reddy, I. K. and Rankin, D., 1973. Magnetotelluric response of a two-dimensional sloping contact by the finite element method. Pure and Applied Geophysics 105, 847-857.

Smith, G. D., 1969. Numerical solution of partial differential equations. Oxford Univ. Press, London.

Weaver, J. T., 1963. The electromagnetic field within a discontinuous conductor with reference to geomagnetic micropulsations near a coastline. Can. J. Physics 41, 484-495.

Weaver, J. T. and Thomson, D. J., 1972. Induction in a non-uniform conducting half-space by an external line current. Geophys. J. R. Astr. Soc. 28, 163-185.

Wright, J. A., 1969. The magnetotelluric and geomagnetic response of two-dimensional structures. Inst. Geophysik und Meteorologie Techn. Univ. Braunschweig. GAMMA 7, 102 S.